materials

MDPI

Article

Structural and Photoluminescence Investigations of Tb^{3+}/Eu^{3+} Co-Doped Silicate Sol-Gel Glass-Ceramics Containing CaF_2 Nanocrystals

Natalia Pawlik [1,*], Barbara Szpikowska-Sroka [1], Tomasz Goryczka [2], Joanna Pisarska [1] and Wojciech A. Pisarski [1]

[1] Institute of Chemistry, University of Silesia, 40-007 Katowice, Poland; barbara.szpikowska-sroka@us.edu.pl (B.S.-S.); joanna.pisarska@us.edu.pl (J.P.); wojciech.pisarski@us.edu.pl (W.A.P.)
[2] Institute of Materials Engineering, University of Silesia, 41-500 Chorzów, Poland; tomasz.goryczka@us.edu.pl
* Correspondence: natalia.pawlik@us.edu.pl; Tel.: +48-32-349-7658

Abstract: In this work, the series of Tb^{3+}/Eu^{3+} co-doped xerogels and derivative glass-ceramics containing CaF_2 nanocrystals were prepared and characterized. The in situ formation of fluoride crystals was verified by an X-ray diffraction technique (XRD) and transmission electron microscopy (TEM). The studies of the Tb^{3+}/Eu^{3+} energy transfer (ET) process were performed based on excitation and emission spectra along with luminescence decay analysis. According to emission spectra recorded under near-ultraviolet (NUV) excitation (351 nm, $^7F_6 \rightarrow {}^5L_9$ transition of Tb^{3+}), the mutual coexistence of the $^5D_4 \rightarrow {}^7F_J$ (J = 6–3) (Tb^{3+}) and the $^5D_0 \rightarrow {}^7F_J$ (J = 0–4) (Eu^{3+}) luminescence bands was clearly observed. The co-doping also resulted in gradual shortening of a lifetime from the $^5D_4$ state of Tb^{3+} ions, and the ET efficiencies were varied from η_{ET} = 11.9% (Tb^{3+}:Eu^{3+} = 1:0.5) to η_{ET} = 22.9% (Tb^{3+}:Eu^{3+} = 1:2) for xerogels, and from η_{ET} = 25.7% (Tb^{3+}:Eu^{3+} = 1:0.5) up to η_{ET} = 67.4% (Tb^{3+}:Eu^{3+} = 1:2) for glass-ceramics. Performed decay analysis from the $^5D_0$ (Eu^{3+}) and the $^5D_4$ (Tb^{3+}) state revealed a correlation with the change in Tb^{3+}–Eu^{3+} and Eu^{3+}–Eu^{3+} interionic distances resulting from both the variable Tb^{3+}:Eu^{3+} molar ratio and their partial segregation in CaF_2 nanophase.

Keywords: Tb^{3+}/Eu^{3+} energy transfer; sol-gel processing; glass-ceramics; fluoride nanocrystals

Citation: Pawlik, N.; Szpikowska-Sroka, B.; Goryczka, T.; Pisarska, J.; Pisarski, W.A. Structural and Photoluminescence Investigations of Tb^{3+}/Eu^{3+} Co-Doped Silicate Sol-Gel Glass-Ceramics Containing CaF_2 Nanocrystals. *Materials* **2021**, *14*, 754. https://doi.org/10.3390/ma14040754

Academic Editor: Paweł Głuchowski
Received: 12 January 2021
Accepted: 2 February 2021
Published: 5 February 2021

1. Introduction

In recent years, the materials doped with rare earths (RE^{3+}) are considered to be indispensable in the development of optoelectronics, offering promising applications in LEDs [1], displays [2], lasers [3], or optical thermometry [4]. The proper adjustment of emission (i.e., generation of appropriate color purity and maintaining suitable luminescence lifetimes) usually requires the involvement of several RE^{3+} ions incorporated into the same host material [5–12]. Indeed, the mutual interactions between them—depending on the concentration of donor and acceptor as well as the type of host—allow for successful tailoring of the above-mentioned optical parameters.

Among numerous combinations of RE^{3+} in doubly- or triply-doped materials, the optical system consisting of Tb^{3+} and Eu^{3+} is a very promising strategy for the generation of multicolor luminescence, which plays a key role in the development of red-green-blue (RGB) optical materials. The Tb^{3+}/Eu^{3+} energy transfer has been extensively explored and described in various types of phosphors, e.g., $LaBWO_6$ [13], $Tb_2MoO_3O_{12}$ [14], $ScPO_4$ [15], or $KAlP_2O_7$ [16]; meanwhile, such studies have not been as common for glass-ceramic materials so far, where Tb^{3+} and Eu^{3+} ions could be distributed between the amorphous glassy host and crystal phase characterized by different decay rates. The evidence of Tb^{3+}/Eu^{3+} ET is stated by the shortening of a lifetime from the $^5D_4$ state of Tb^{3+} in the

presence of acceptor ions (Eu^{3+}). It is reported in the literature that the fluorescence decay becomes quicker with the increment of Eu^{3+} content, which accelerates the Tb^{3+}/Eu^{3+} ET and makes it more efficient [17–22]. Furthermore, a comparative analysis of energy transfer efficiency, η_{ET}, in precursor glasses and glass-ceramics is also carried out to demonstrate the impact of controlled crystallization on Tb^{3+}/Eu^{3+} ET. Such studies were performed in excellent work by Chen et al. [19] for $44SiO_2$-$28Al_2O_3$-17NaF-(10-x)YF_3-$1TbF_3$-xEuF_3 (x = 0, 0.1, 0.25, 0.5, 1) (mol%) glasses and derivative glass-ceramics fabricated at 670 °C. The η_{ET} for a glass containing 0.1 mol% Eu^{3+} achieved as low value as 1.39%, which finally grew to 30.28% for a glass containing 1 mol% Eu^{3+}. Further, the authors have clearly proven that a crucial role in Tb^{3+}/Eu^{3+} ET plays is glass crystallization, which results in significant growth in η_{ET} values from 16.63% (for glass-ceramic containing 0.1 mol% Eu^{3+}) up to 47.70% (for glass-ceramic containing 1 mol% Eu^{3+}). Similarly, an impact of controlled ceramization on Tb^{3+}/Eu^{3+} ET behavior was also studied by Hu et al. [21], who found that η_{ET} increased from 8.7% for glasses with composition $45SiO_2$-$20Al_2O_3$-10CaO-24.04CaF_2-0.05TbF_3-0.01EuF_3 (mol%) up to 14.0% for nano-glass-ceramic produced at 700 °C.

It should be pointed out that the majority of glass-ceramics containing Tb^{3+} and Eu^{3+} ions characterized and described in literature was prepared by the conventional melt-quenching method followed by controlled heat-treatment at the specified conditions of time and temperature [17–19,21–26]. An alternative route to the fabrication of glass-ceramics is the sol-gel technique, which offers quite easy fabrication of materials with complex compositions, which could be difficult to obtain via the melt-quenching technique [27–31]. Moreover, particular research attention has been focused on oxyfluoride glass-ceramics, which possess higher chemical and mechanical stability than fluoride glasses and lower phonon energies than oxide glasses. Among fluorides, the calcium fluoride, CaF_2, is an optically isotropic crystal characterized by a broad region of transparency from 0.13 up to 9.5 μm, wide bandgap (12 eV), and relatively low phonon energy (~466 cm^{-1}) [32–34]. Those features of CaF_2 crystals are urgent to be a suitable medium for optically active rare earths, widely dedicated to fulfilling many sophisticated, active functions for opto-electronics. Indeed, the optical materials based on the CaF_2 phase are frequently applied to generate an efficient up- [35] and down-conversion luminescence [36] or white light emission [37]. Therefore, such materials could be successfully predisposed for use in laser technologies [38], bio-imaging [39], or to increase the efficiency of solar cells [40]. Moreover, according to our previous results for sol-gel nano-glass-ceramics containing divalent metals fluorides, MF_2 (M = Ca, Sr, Ba), singly-doped with Eu^{3+} ions, the most efficient segregation of Eu^{3+} inside fluoride crystal lattice, was reported for the SiO_2-CaF_2 system [41–43]. Indeed, a clear correlation was observed between the average decay time of the $^5D_0$ state and growing difference in ionic radius of Eu^{3+} and each of individual M^{2+} cation in the following order: $Ca^{2+} \rightarrow Sr^{2+} \rightarrow Ba^{2+}$ (SiO_2-CaF_2:Eu^{3+}: τ_{avg} = 11.92; SiO_2-SrF_2:Eu^{3+}: τ_{avg} = 7.77; SiO_2-BaF_2:Eu^{3+}: τ_{avg} = 4.08 ms). Therefore, due to the efficient and long-lived luminescence in fabricated SiO_2-CaF_2:Eu^{3+} nano-glass-ceramics, it seems that this material could be considered as a very promising host to study the Tb^{3+}/Eu^{3+} ET. Indeed, we reported interesting results for Tb^{3+}/Eu^{3+} ET for sol-gel systems containing selected trivalent metals fluorides, MF_3 (M = Y, La) [44]; hence, we performed such measurements for nano-glass-ceramics with divalent metal fluoride, CaF_2. Moreover, to the best of our knowledge, the investigation of Tb^{3+}/Eu^{3+} ET in oxyfluoride sol-gel glass-ceramics is rarely described in the available literature. Indeed, it was examined only in SiO_2-SrF_2 [20] and SiO_2-$BaGdF_5$ [45] sol-gel nano-glass-ceramics; however, there are no reports on the SiO_2-CaF_2 system so far. Due to the above reasons, it seems justified to study the Tb^{3+}/Eu^{3+} ET in silicate sol-gel glass-ceramics containing CaF_2 nanocrystals.

In this work, we fabricated and examined the series of sol-gel SiO_2-CaF_2 nano-glass-ceramics co-doped with Tb^{3+} and Eu^{3+} ions with the variable Tb^{3+}:Eu^{3+} molar ratio (0.05:x, where x = 0.025, 0.05, 0.075, 0.1). The CaF_2 phase was obtained via in situ crystallization from $Ca(CF_3COO)_2$ at as low a temperature as 350 °C, and its presence was verified using

XRD measurements and TEM microscopy. The changes in photoluminescence behavior of fabricated sol-gel materials have been described in association with the variable Tb^{3+}:Eu^{3+} molar ratio, as well as the structural transformation from amorphous xerogels into nano-glass-ceramics. Based on photoluminescence results, the interactions between Tb^{3+} and Eu^{3+} ions were systematically investigated. Indeed, a clear correlation was observed between the R/G ratio and energy transfer efficiency (η_{ET}), as well as decay times of the $^5D_4$ state (Tb^{3+}) as the Tb^{3+}:Eu^{3+} molar ratio gradually decreased. Additionally, the lifetimes of the $^5D_0$ excited level of Eu^{3+} ions were also determined. The obtained sol-gel materials exhibited bright multicolor luminescence tuned when the Tb^{3+}:Eu^{3+} molar ratio was changed.

2. Materials and Methods

The series of xerogels co-doped with Tb^{3+} and Eu^{3+} ions were synthesized using the sol-gel method described elsewhere [41,46]. All reagents were taken from Sigma Aldrich Chemical Company (St. Louis, MO, USA). After pre-hydrolysis of the mixture containing TEOS, ethyl alcohol, deionized water, and acetic acid in molar ratio equals 1:4:10:0.5 (90 wt.%), the solutions of $Ca(CH_3COO)_2$, $Tb(CH_3COO)_3$, and $Eu(CH_3COO)_3$ in water and trifluoroacetic acid (TFA) were added dropwise. For each sol-gel sample, a mixture of TFA and acetates was 10 wt.%, and the molar ratio equaled TFA:$Ca(CH_3COO)_2$:$Tb(CH_3COO)_3$:$Eu(CH_3COO)_3$ = 5:1:0.05:x (where x = 0, 0.025, 0.05, 0.075, and 0.1). The obtained sols were dried at 35 °C for seven weeks to form solid xerogels. The following xerogel samples were denoted as follows: $XG_{1Tb0.5Eu}$ (x = 0.025), XG_{1Tb1Eu} (x = 0.05), $XG_{1Tb1.5Eu}$ (x = 0.075), and XG_{1Tb2Eu} (x = 0.1). The glass-ceramic materials were obtained by controlled heat-treatment at 350 °C for 10 h. Such glass-ceramics were denoted as appropriate GC samples: $GC_{1Tb0.5Eu}$, GC_{1Tb1Eu}, $GC_{1Tb1.5Eu}$, GC_{1Tb2Eu}. The sol-gel samples singly-doped with Tb^{3+} ions were also prepared (XG_{1Tb}, GC_{1Tb}) to compare with the luminescence properties of Tb^{3+}/Eu^{3+} co-doped materials.

The sol-gel network's vibrational modes were identified using the Nicolet iS50 ATR spectrometer (Thermo Fisher Scientific, Waltham, MA, USA) in a frequency region 500–4000 cm^{-1}. The X-ray diffraction analysis of fabricated xerogels and glass-ceramics was performed using an X'Pert Pro diffractometer supplied by PANalytical with CuK_α radiation (Almelo, The Netherlands). The microstructure of fabricated glass-ceramics was observed using the JEOL JEM 3010 electron transmission microscope operated at 300 kV (JEOL JEM 3010, Tokyo, Japan). The excitation and emission spectra, as well as luminescence decay curves were recorded on Horiba Jobin Yvon FluoroMax-4 spectrofluorimeter supplied with 150 W Xe lamp (Horiba Jobin Yvon, Longjumeau, France). The spectra were recorded with 0.1 nm resolution, and the decay curves were recorded with 2 µs accuracy. All structural and luminescence measurements were carried out at room temperature.

3. Results and Discussion

3.1. Structural Characterization: XRD, TEM, and IR Spectroscopy

In general, fabricated sol-gel materials' structural properties strongly determine the local environment around Tb^{3+} and Eu^{3+}, which are crucial in understanding any changes in their photoluminescence behavior (i.e., emission spectra and decay profiles). The detailed studies in this aspect (the structural evolution from sols, through gels, and xerogels, up to nano-glass-ceramics) were systematically investigated and described for the similar SiO_2-LaF_3:Eu^{3+} system in our previous work [47]. Therefore, to explain the luminescence features of fabricated SiO_2-CaF_2:Tb^{3+}, Eu^{3+} samples, a brief comment on their structural properties was also presented below.

The performed heat-treatment of xerogels is responsible for both in situ crystallization of CaF_2 nanophase (verified by XRD and TEM measurements, Figure 1) and evolution of the silicate sol-gel network (indicated by IR-ATR measurements, Figure 2). Such measurements were performed for representative XG_{1Tb1Eu} and GC_{1Tb1Eu} co-doped samples. As was demonstrated in Figure 1, a broad halo pattern was recorded for xerogel, which

indicates an amorphous nature without long-range structural order. The diffraction reflexes characteristic for the CaF_2 phase crystallized in Fm3m space group (ICDD, PDF-2 No. 65-0.0535) were observed after controlled ceramization. The broadening of recorded diffraction lines indicates the crystallization of the CaF_2 phase in nanoscale, the average crystal size of which was estimated to be 8.1 ± 0.4 nm from the Scherrer formula:

$$D = \frac{K\lambda}{B\cos\theta} \quad (1)$$

where D is the crystal size, K is a constant value (in our calculations, we took K = 1), λ is the X-ray wavelength (1.54056 Å, CuK_α), B is a half of the diffraction line, and θ is the diffraction angle [48]. Another method that allowed us to determine the crystallites' size, which is an extension of the Scherrer equation, was the Williamson–Hall method, based on plotting the following dependence for several reflexes derived from the same crystalline phase:

$$\beta\cos\theta = \frac{K\lambda}{D} + 4\left(\frac{\Delta a}{a}\right)\sin\theta \quad (2)$$

in which β is a half of the diffraction line and (Δa/a) refers to the lattice deformation [49]. From the Williamson–Hall plot's linear fit, the crystallite size was estimated to be 16.6 ± 1.5 nm (the "chi-square" regression coefficient was equaled to 0.97). Since the Williamson–Hall approach considers crystal imperfections and lattice distortion, as well as apparatus factors, this method allowed us to determine the mean crystallite size more reliably than the Scherrer method (indeed, the latter does not consider such distortions of the crystal lattice). Indeed, the size of CaF_2 nanocrystals from the TEM image (inset of Figure 1) was in more prominent agreement with the data obtained by the Williamson–Hall method (16.6 ± 1.5 nm) than by the Scherrer equation (8.1 ± 0.4 nm). It should be noted that the average crystal size estimated by the Williamson–Hall method was two-fold larger than from the Scherrer equation. Taking into account the factors related to the prepared sample itself, we suppose that one of the reasons for the discrepancy in the values estimated by various methods, apart from the differences in the ionic radii of Ca^{2+} (1.00 Å) [50], Tb^{3+} (1.04 Å), and Eu^{3+} (1.07 Å) [51], could be related to the charge compensation when trivalent cations were substituting divalent Ca^{2+} in the CaF_2 crystal lattice. Indeed, to balance an excess of the positive charge introduced by the RE^{3+} ion, the F^- anions were distributed in interstitial positions [52]. Such interstitial F^- anions induced a local distortion in the crystal lattice due to the repulsion between them. Therefore, we assumed that the charge compensation effect might contribute to the identified difference in crystal size.

Besides the crystallization of the CaF_2 nanophase, the track of structural changes inside the sol-gel host is also important to explain Tb^{3+} and Eu^{3+} dopant ions' luminescence properties. The sol-gel systems were dynamic during controlled heat-treatment at 350 °C performed for the next 10 h because it induced evaporation of residual solvents (water and organic liquids) from a microporous structure and polycondensation reaction with the participation of Q^2 ($[Si(O_{1/2})_2O_2]^{-2}$), Q^3 ($[Si(O_{1/2})_3O]^-$), and Q^4 units ($[Si(O_{1/2})_4]$) (in the description "$O_{1/2}$" is corresponding to each oxygen atom, which is involved in the formation of Si–O–Si bridge; however, "O" is according to a non-bridging oxygen atom; therefore higher value of "n" index is, the less Si–OH unreacted groups are). To examine such structural evolution, the IR-ATR spectra were recorded in the frequency region from 500 to 4000 cm^{-1} (Figure 2), and the bands were assigned to appropriate vibrational modes based on literature data [53–58]. Generally, we distinguished three primary regions classified by the functional groups causing the characteristic vibrations: 3750–2500 cm^{-1} (OH groups and C–H bond), 1820–1510 cm^{-1} (C=O bond, Si–OH groups, and adsorbed H_2O), and 1275–500 cm^{-1} (silicate host). For a more in-depth interpretation of oscillations that occurred in the sol-gel network, deconvolution was performed. The peak fitting during the deconvolution was done using a Gauss function with a squared regression coefficient of $R^2 \geq 0.998$.

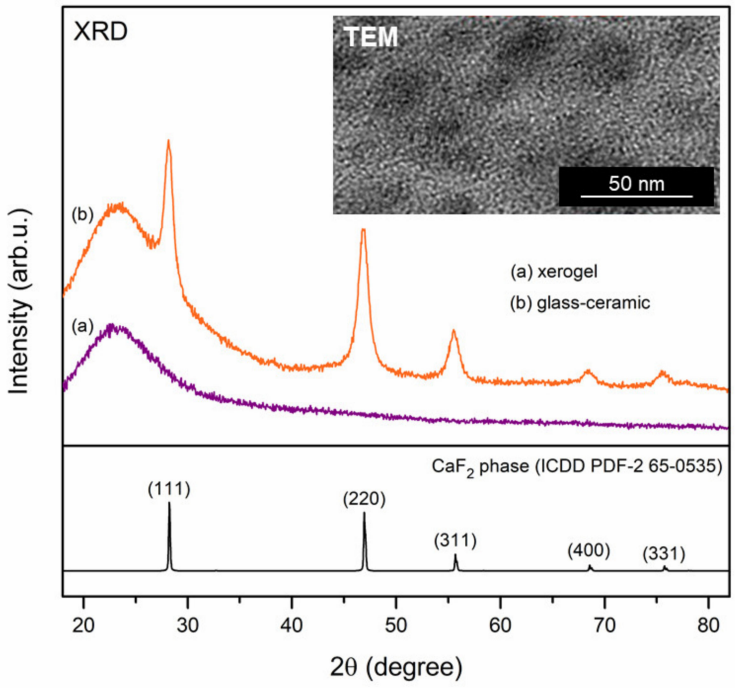

Figure 1. XRD patterns of XG_{1Tb1Eu} and GC_{1Tb1Eu} co-doped sol-gel materials. Inset shows the TEM image of glass-ceramic fabricated at 350 °C.

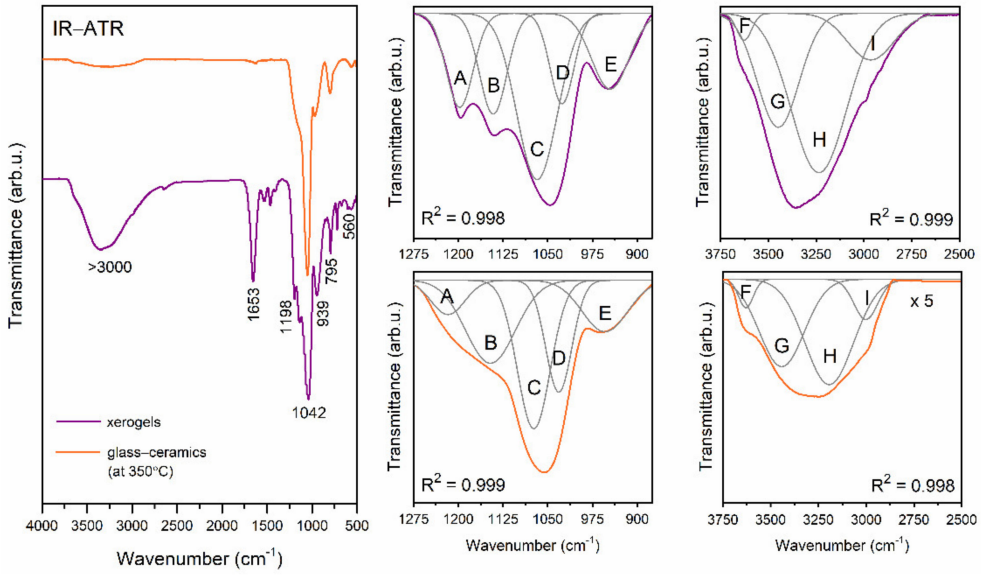

Figure 2. IR-ATR spectra recorded for xerogels and glass-ceramics. The deconvolution of bands characteristic for silicate host (1275–875 cm^{-1}) as well as OH moieties and C–H bonds (3750–2500 cm^{-1}) was also presented.

Firstly, we analyzed the origin of deconvoluted bands (denoted as A–E) identified within the 1275–620 cm^{-1} spectral region. It was established that band A (~1200 cm^{-1}) was corresponding to the TO_4 mode of created Si–O–Si siloxane bridges, band B (~1140 cm^{-1}) was correlated with oscillations within Q^4 structural units ($[Si(O_{1/2})_4]$), and band C (~1070 cm^{-1}) could be associated with the TO_3 mode of Si–O–Si siloxane bridges. Bands D (~1030 cm^{-1}) and E (~960 cm^{-1}) were related to Q^3 and Q^2 units' oscillations, respectively [53,54,56]. According to the literature, bands A and B could also be interpreted as vibrations originated from the C–F bond inside $–CF_3$ groups in trifluoroacetates [55]. It was clearly visible that the intensities of bands A, B, and E decreased during the transformation

of xerogels into glass-ceramics. Indeed, since $Ca(CF_3COO)_2$ underwent thermal decomposition during controlled ceramization [41], the vibrations from the C–F bond disappeared for glass-ceramics, and bands A and B should have originated only from vibrations inside the Si–O–Si siloxane bridges. Further, a decrease in the intensity of band E clearly pointed to the conversion of Q^2 structural units into Q^n (n = 3, 4) units as a consequence of polycondensation reaction. The additional weak bands located at the 616 and 561 cm^{-1} frequency region indicated some cyclic structures inside the sol-gel host [53,56].

Finally, we analyzed the broad band recorded in a frequency region from 3750 up to 2500 cm^{-1}. The deconvolution revealed the presence of three bands originated from different types of OH moieties: Geminal or vicinal Si–OH groups (~3630 cm^{-1}, band F), hydrogen-bonded Si–OH groups (~3450 cm^{-1}, band G), and hydrogen-bonded OH groups originated from residual water and organic compounds (~3200 cm^{-1}, band H). It should be noted that deconvolution also revealed the fourth component band (~2990 cm^{-1}, band I), which corresponded to the vibrations of C–H bonds [53,54,56]. It was observed that an indicated broad band was much more intense for xerogels than for glass-ceramics (indeed, to show the deconvolution better, the band's intensity was fivefold enlarged). In fact, such a relatively strong band for xerogels was a consequence of "trapping" of water and organic liquids inside pores via hydrogen-bonding created with unreacted Si–OH groups. During ceramization, the band was significantly reduced, which clearly evidenced successful evaporation of water and organic liquids as well as a continuation of polycondensation reaction. The conclusions from the above observations could also be confirmed by the behavior of the infrared signal located at ~1660 cm^{-1}, which was attributed to the vibrations of the C=O bond, Si–OH surface groups, and adsorbed water [55,57,58]. The indicated band was well-observable for xerogels, and it almost completely disappeared for glass-ceramics. According to IR and XRD results, the graphical visualization of sol-gel evolution during performed ceramization at 350 °C, as presented in Figure 3.

3.2. Luminescence Properties of Fabricated Sol-Gel Materials

3.2.1. Determination of Local Symmetry Using Spectroscopy of Eu^{3+} Ions as Spectral Probes

The emission spectra recorded for fabricated XG_{1TbxEu} xerogels using λ_{exc} = 395 nm excitation line were shown in Figure 4. The characteristic $^5D_0 \rightarrow {}^7F_J$ luminescence bands of Eu^{3+} ions were detected in the reddish-orange light area and their maxima were located at following wavelengths: 578 (J = 0), 592 (J = 1), 615 (J = 2), 647 (J = 3), and 698 nm (J = 4). A gradual increase in their intensity was observed, when the Tb^{3+}:Eu^{3+} molar ratio systematically changed from 1:0.5 to 1:2. It is clearly visible that among series of recorded bands, the $^5D_0 \rightarrow {}^7F_2$ one was the most prominent line for all xerogels before their controlled ceramization, despite the Tb^{3+}:Eu^{3+} molar ratio. Indeed, Eu^{3+} ions were frequently used as spectral probes due to the characteristic nature of their transitions. The $^5D_0 \rightarrow {}^7F_1$ is a magnetic-dipole transition (MD) in nature, the intensity of which is rather independent of the host. In contrast, the $^5D_0 \rightarrow {}^7F_{0.2–4}$ are electric-dipole transitions (ED) known to be forbidden by the Laporte selection rule and may occur due to mixing the 4f orbitals with the opposite parity at the low-symmetry sites. Among ED transitions, the $^5D_0 \rightarrow {}^7F_2$ one has a hypersensitive nature, and its intensity is easily affected by the local vicinity: It is promoted in low-symmetric frameworks; meanwhile, it is inhibited in more symmetric environments. Hence, we could infer about the symmetry based on the ratio of integrated intensities of the bands mentioned above, which is well-known in literature as the R/O ratio ($I(^5D_0 \rightarrow {}^7F_2)/I(^5D_0 \rightarrow {}^7F_1)$) [59,60]. XRD results confirmed the amorphous nature of xerogels without long-range order, so we expected relatively high asymmetry in the immediate vicinity of Eu^{3+}. Indeed, the calculated R/O ratio values hesitated from 3.50 (XG_{1Tb2Eu}) to 3.91 ($XG_{1Tb0.5Eu}$). On this occasion, it should also be noted that comparability in calculated R/O ratio values clearly pointed to a chemically similar environment of Eu^{3+} ions in all synthesized xerogels.

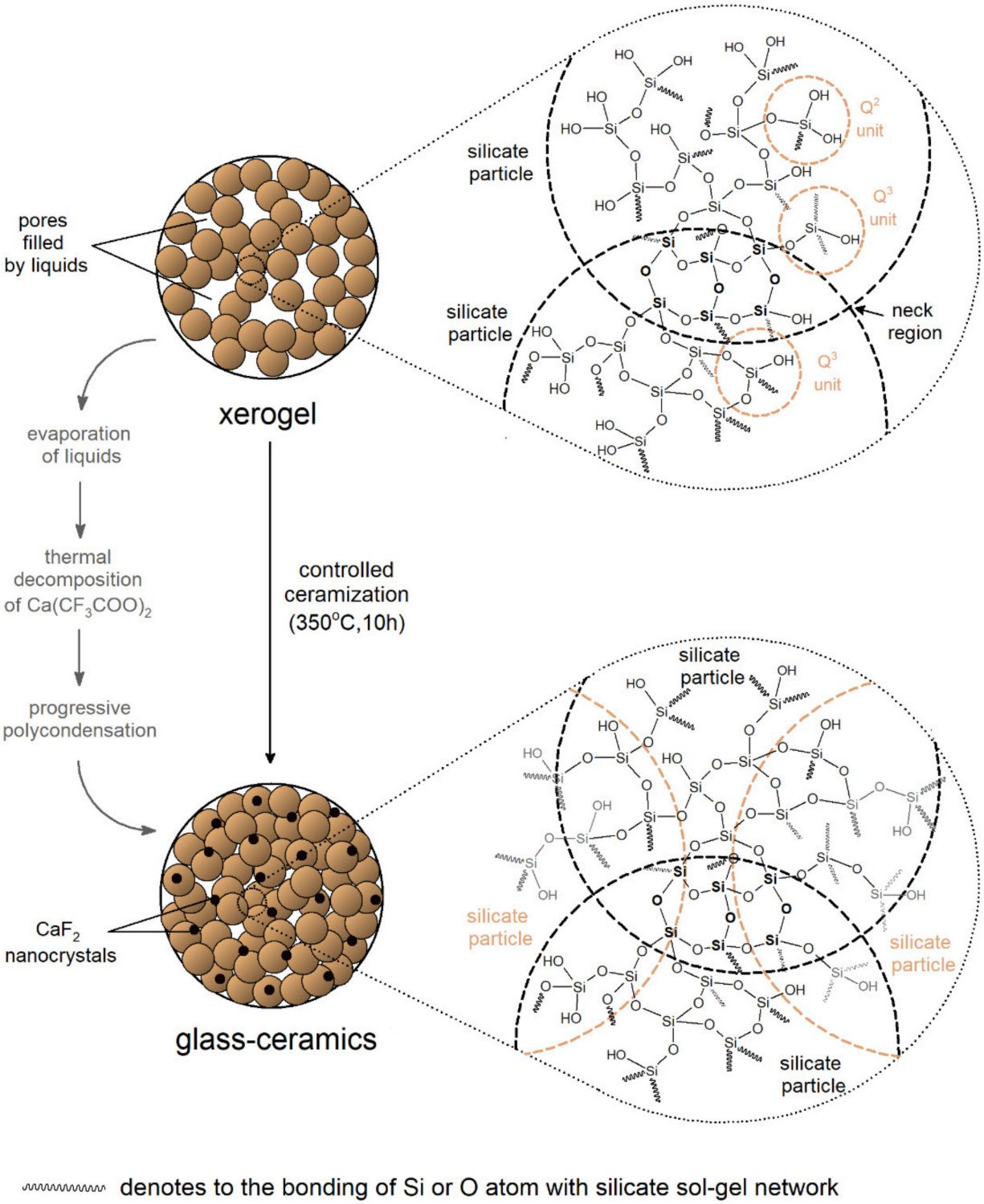

Figure 3. Graphical representation of structural transformation during controlled ceramization at 350 °C.

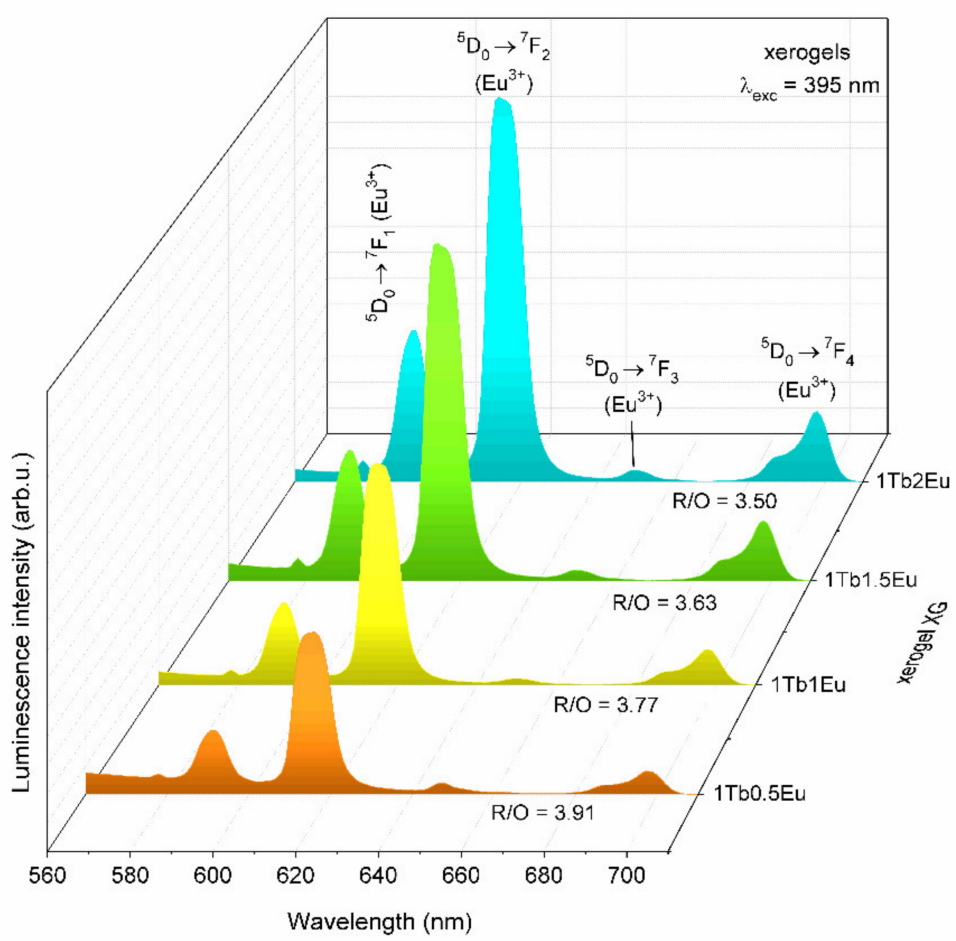

Figure 4. The emission spectra of XG_{1TbxEu} xerogels co-doped with Tb^{3+}/Eu^{3+} ions recorded at λ_{exc} = 395 nm.

The emission spectra recorded for GC_{1TbxEu} glass-ceramics upon excitation at λ_{exc} = 394 nm were presented in Figure 5. Similar as for xerogels, a series of characteristic bands corresponding to the intraconfigurational transitions within $4f^6$ manifold were registered: $^5D_0 \rightarrow {}^7F_0$ (577), $^5D_0 \rightarrow {}^7F_1$ (592), $^5D_0 \rightarrow {}^7F_2$ (612), $^5D_0 \rightarrow {}^7F_3$ (648) and $^5D_0 \rightarrow {}^7F_4$ (683/689/698 nm). It was clearly observed that the intensity of the emission bands successfully increased with the growing content of Eu^{3+} ions (as the Tb^{3+}:Eu^{3+} molar ratio changed from 1:0.5 to 1:2). For each glass-ceramic, the orange emission band corresponding to the $^5D_0 \rightarrow {}^7F_1$ MD transition maintained the greatest intensity and dominated the $^5D_0 \rightarrow {}^7F_2$ ED red band. Generally, an almost six-fold decline of R/O ratio value was observed, which equaled close to 0.64 after controlled ceramization (compared with xerogels for which the R/O ratio value was approximately equal to 3.70). Hence, such a decrease in the R/O ratio value pointed to significant changes in the symmetry in the immediate vicinity of Eu^{3+} ions, as well as a change in the nature of the bonding character from covalent to more ionic [61]. When the nearest framework of Eu^{3+} ions was more symmetric (which usually accompanied the migration of Eu^{3+} from an asymmetric amorphous structure without long-range order to crystalline lattice), the probability of the $^5D_0 \rightarrow {}^7F_{0,2-4}$ electric-dipole transitions successfully decreased [60]. Indeed, the identified decrease in the R/O ratio value was strictly accompanied by partially entering of optically active ions into precipitated CaF_2 fluoride crystal fraction with long-range order. In other words, such a decline was direct evidence that Ca^{2+} cations from fluoride crystal lattice were successfully substituted by Eu^{3+} ions. It should also be noted that a Stark splitting characteristic in the crystal-field was not observed because part of the Eu^{3+} ions was still distributed in an amorphous sol-gel host [60].

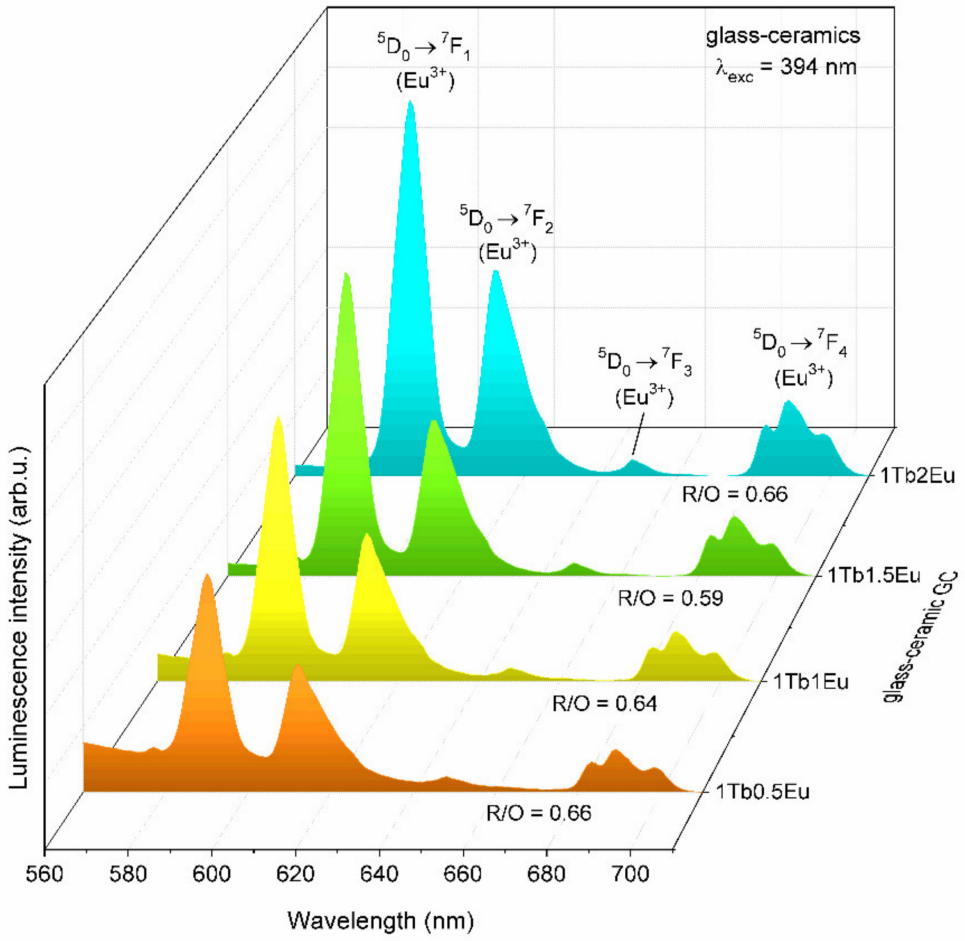

Figure 5. The emission spectra of GC_{1TbxEu} glass-ceramics co-doped with Tb^{3+}/Eu^{3+} ions recorded at λ_{exc} = 394 nm.

3.2.2. Studies of Tb^{3+}/Eu^{3+} Energy Transfer in Sol-Gel Materials with the Variable Tb^{3+}:Eu^{3+} Molar Ratio

To select the excitation line appropriate for Tb^{3+}/Eu^{3+} ET studies, the photoluminescence excitation spectra for XG_{1Tb1Eu} co-doped representative xerogel were presented in Figure 6. The spectra were recorded for λ_{em} = 543 and λ_{em} = 612 nm emissions of Tb^{3+} (the $^5D_4 \rightarrow {}^7F_5$ green line), and Eu^{3+} (the $^5D_0 \rightarrow {}^7F_2$ red line), respectively. The recorded excitation bands of Tb^{3+} ions were associated to the following f-f intraconfigurational transitions: $^7F_6 \rightarrow {}^5L_9$ (352), $^7F_6 \rightarrow {}^5L_{10}$ (370), $^7F_6 \rightarrow {}^5D_3$ (379), as well as $^7F_6 \rightarrow {}^5D_4$ (487 nm). Simultaneously, the recorded bands were ascribed to the transitions of Eu^{3+} ions from the $^7F_0$ ground state into the subsequent higher energy levels: $^5D_4$ (363), ^5G_J, $^5L_7$ (from 371 to 390), $^5L_6$ (395), and $^5D_2$ (465 nm). Since the $^7F_6 \rightarrow {}^5L_9$ transition of Tb^{3+} ions did not coincide with any excitation peak of Eu^{3+}, we decided to select the λ_{exc} = 351 nm excitation line to study the Tb^{3+}/Eu^{3+} ET process.

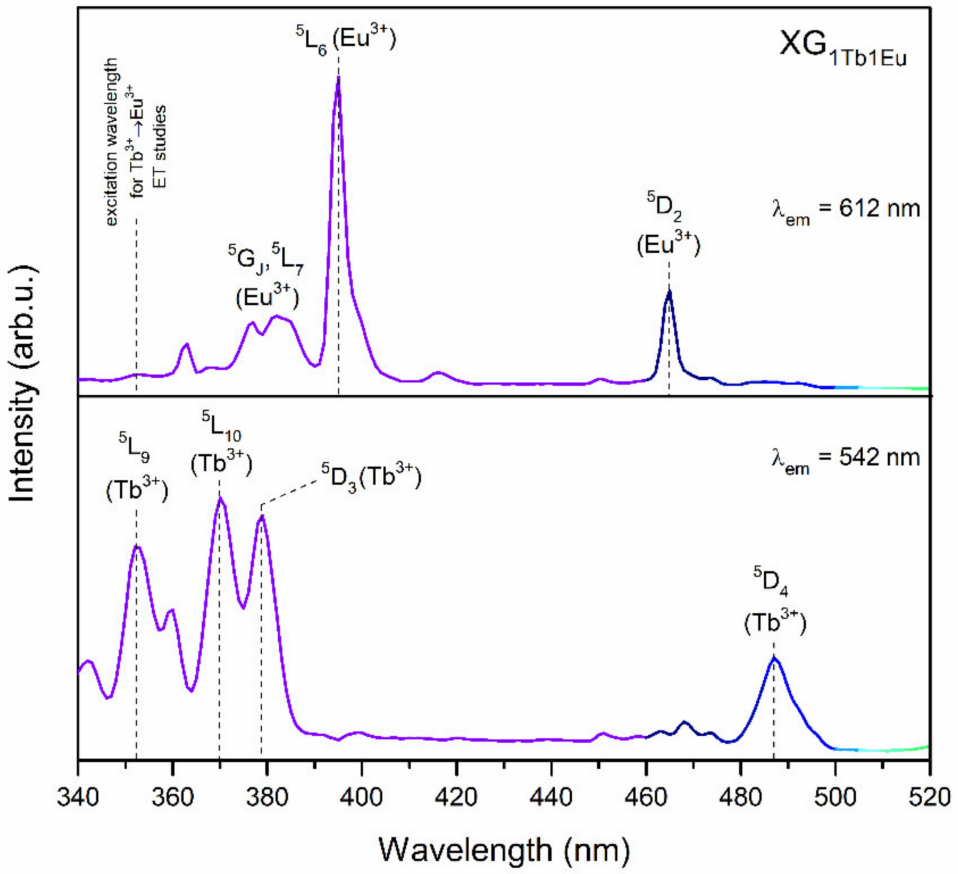

Figure 6. Excitation spectra recorded for red (λ_{em} = 612) and green (λ_{em} = 542 nm) emission lines for XG_{1Tb1Eu} xerogel.

The photoluminescence spectra recorded for XG_{1Tb} xerogel (upon excitation at λ_{exc} = 351 nm wavelength) as well as for the XG_{1Tb1Eu} co-doped representative sample (recorded under excitation at λ_{exc} = 395 and λ_{exc} = 351 nm lines) are depicted in Figure 7. The spectra recorded for the XG_{1Tb} sample revealed two emission bands in bluish-green spectral scope, i.e., $^5D_4 \rightarrow {}^7F_6$ (488) and $^5D_4 \rightarrow {}^7F_5$ (542 nm) of the predominant intensity, as well as two other emission bands of Tb^{3+} ions in the yellowish-red area: $^5D_4 \rightarrow {}^7F_4$ (582) and $^5D_4 \rightarrow {}^7F_3$ (620 nm). When the XG_{1Tb1Eu} co-doped sample was excited by the λ_{exc} = 395 nm line, only the characteristic $4f^6$-$4f^6$ emission bands originated from Eu^{3+} ions ($^5D_0 \rightarrow {}^7F_J$, J = 0–4) were recorded. A tune in the excitation wavelength to λ_{exc} = 351 nm also led to the generation of the characteristic emission lines of Tb^{3+} ions. Such coexistence of emission lines originated from both optically active dopants is due to the energy transfer process from Tb^{3+} to Eu^{3+} [17–22]. In the case of the band recorded in a red spectral scope, a slight shift was observed of a maximum from 620 (XG_{1Tb}) to 618 nm (XG_{1Tb1Eu}), which was caused by overlapping the weak $^5D_0 \rightarrow {}^7F_2$ band of Eu^{3+} ions (with a maximum at 615 nm) with the $^5D_4 \rightarrow {}^7F_3$ band of Tb^{3+} ions (with a maximum at 620 nm). In general, the spectral matching of the donor's emission (Tb^{3+}) and the acceptor's excitation (Eu^{3+}) regions was a fundamental condition for energy transfer occurrence [62]. In this way, upon irradiation using the λ_{exc} = 351 nm line from NUV spectral region, Tb^{3+} ions could be successfully pumped into the $^5L_9$ level, and then, the non-radiative de-activation to the $^5D_4$ state took place. The excitation energy from the $^5D_4$ state (Tb^{3+}) could be successfully transferred into the $^5D_1$ or the $^5D_0$ level (Eu^{3+}). Hence, among characteristic emission lines from Tb^{3+} ions, additional bands originated from Eu^{3+} can also be recorded.

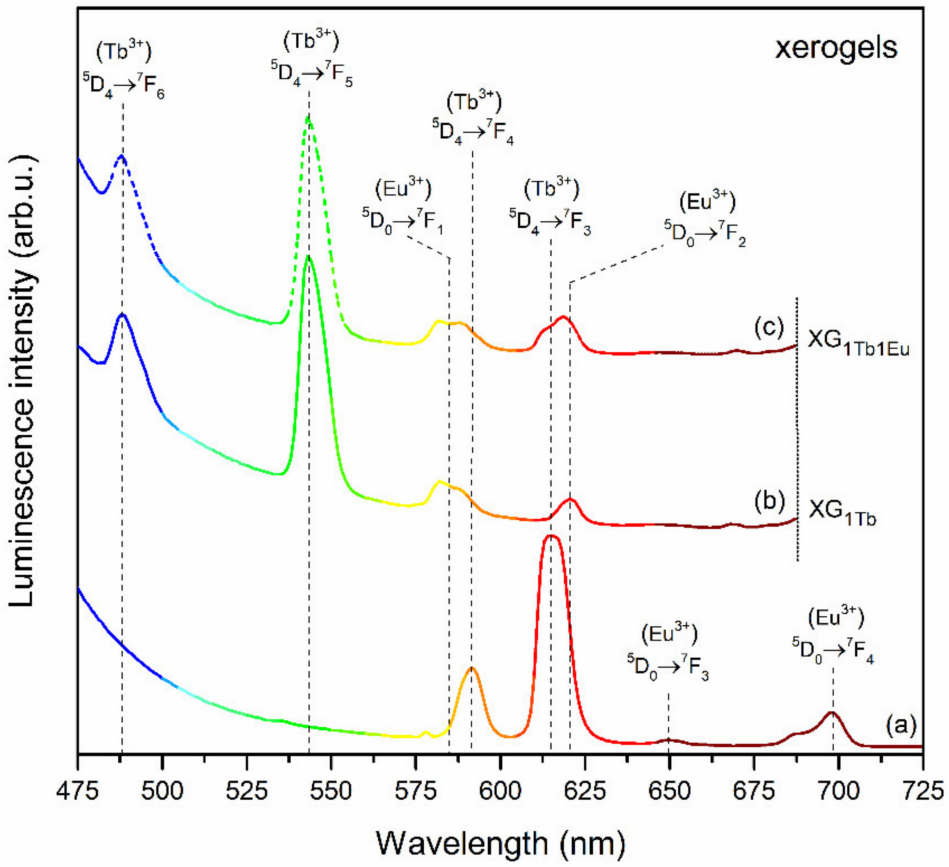

Figure 7. Emission spectra of: (**a**) XG_{1Tb1Eu} (λ_{exc} = 395), (**b**) XG_{1Tb} (λ_{exc} = 351), and (**c**) XG_{1Tb1Eu} (λ_{exc} = 351 nm).

The emission spectra of Tb^{3+}/Eu^{3+} co-doped xerogels with the varying Tb^{3+}:Eu^{3+} molar ratio recorded upon excitation at λ_{exc} = 351 nm are presented in Figure 8. A slight decrease was observed in the emission intensity of the $^5D_4 \rightarrow {}^7F_6$ and the $^5D_4 \rightarrow {}^7F_5$ bands of Tb^{3+} ions when the Tb^{3+}:Eu^{3+} molar ratio gradually decreases. Hence, the R/G ratio values ($(I(^5D_0 \rightarrow {}^7F_2)(Eu^{3+})+I(^5D_4 \rightarrow {}^7F_3)(Tb^{3+})/I(^5D_4 \rightarrow {}^7F_5)(Tb^{3+})$) were estimated. For the XG_{1Tb} sample, the R/G ratio was defined as the ratio of integrated intensities of the $^5D_4 \rightarrow {}^7F_3$ red band and the $^5D_4 \rightarrow {}^7F_5$ green emission line [63]. In the case of the XG_{1TbxEu} co-doped samples, an additional contribution of luminescence originated from Eu^{3+} ions into total red emission should also be taken into account. Hence, the R/G ratio was calculated as $(I(^5D_4 \rightarrow {}^7F_3)(Tb^{3+}) +I(^5D_0 \rightarrow {}^7F_2)(Eu^{3+})/I(^5D_4 \rightarrow {}^7F_5)(Tb^{3+}))$ and its increase can be interpreted as a growing share of Eu^{3+} ions in total generated multicolor luminescence. Indeed, a slight increase in R/G ratio values was determined in the following order: From 0.09 (XG_{1Tb}), through 0.15 ($XG_{1Tb0.5Eu}$), 0.17 (XG_{1Tb1Eu}), 0.26 ($XG_{1Tb1.5Eu}$), to 0.30 (XG_{1Tb2Eu}). Such an increment of the R/G ratio suggests more efficient Tb^{3+}/Eu^{3+} ET when the Eu^{3+} content gradually grew, since the Tb^{3+}:Eu^{3+} molar ratio changed from 1:0.5 to 1:2. Nevertheless, such a small increase in the R/G ratio resulted from the relatively large interionic distances between Tb^{3+} and Eu^{3+} ions, characteristic for the amorphous xerogel host.

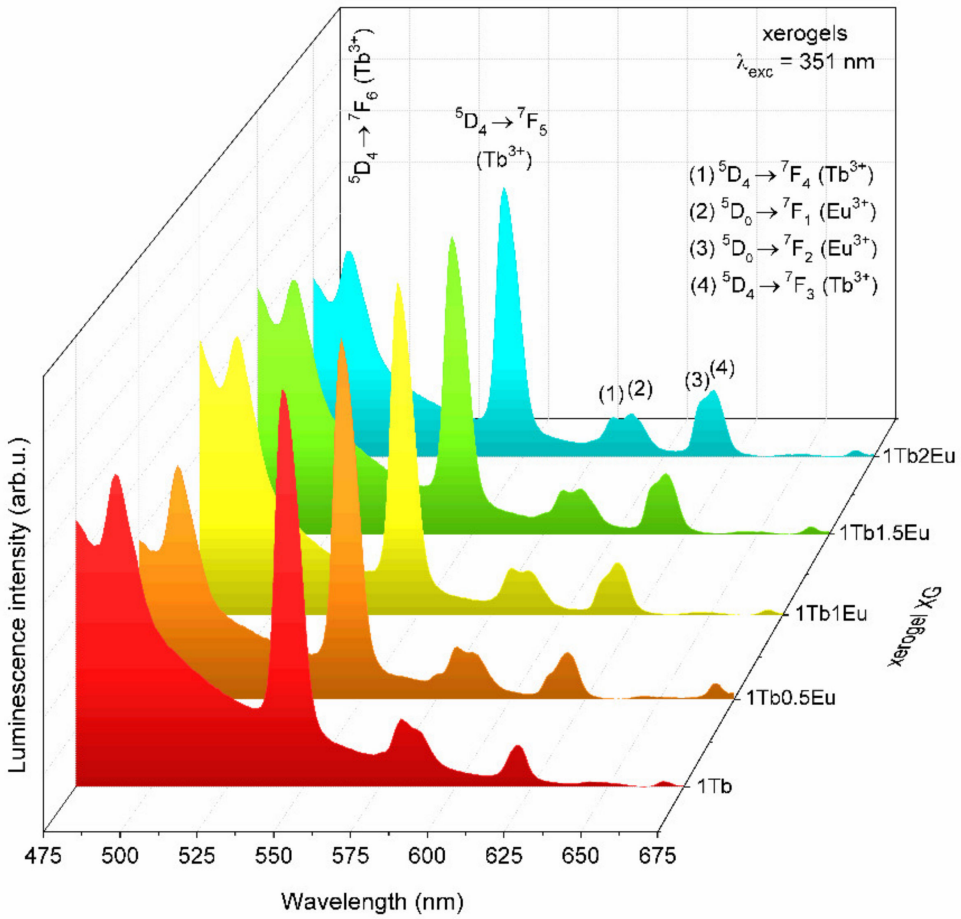

Figure 8. The emission spectra of XG_{1Tb} and XG_{1TbxEu} xerogels recorded under excitation at λ_{exc} = 351 nm.

Additionally, an increasing background for prepared sol-gel samples was also observed, especially at wavelengths <540 nm. Such a background was associated with the wide band from the silicate sol-gel host, as was shown by other authors, e.g., Tomina et al. [64], for different types of Eu^{3+}-loaded aminosilica spherical particles. The authors suggest that such a band could result, i.e., from the charge transfer on Si-O bonds or defect from the silicate network. They have proven that such a wide band's intensity is strictly related to the type of complexes formed by Eu^{3+} ions with amine ligands connected with the silicate sol-gel host. A similar effect was reported by Kłonkowski et al. [20], who synthesized sol-gel glass-ceramics containing SrF_2 singly- and doubly-doped with Tb^{3+}/Eu^{3+}. The broad band's origin was explained by defects, like dangling bonds, inside silicate sol-gel host.

The emission spectra recorded for GC_{1Tb} (upon excitation at λ_{exc} = 351 nm wavelength) and GC_{1Tb1Eu} co-doped the representative sample (recorded under excitation at λ_{exc} = 394 nm and λ_{exc} = 351 nm lines) are depicted in Figure 9. Similarly as for xerogel, for the GC_{1Tb} sample, the characteristic emission bands corresponding to the transitions from the $^5D_4$ excited level into the $^7F_6$ (488), $^7F_5$ (542), $^7F_4$ (581), and $^7F_3$ (621 nm) lower-lying states were detected. In the case of the GC_{1Tb1Eu} sample, the coexistence of the luminescence lines originating from both rare-earth dopants was clearly observed after excitation at λ_{exc} = 351 nm line. Therefore, an appearance of characteristic emission bands coming from Eu^{3+} ions upon excitation of Tb^{3+} confirmed the occurrence of Tb^{3+}/Eu^{3+} ET. It should be particularly pointed out that the intensity of Tb^{3+} emission strongly decreased, accompanied by significant enhancement of Eu^{3+} luminescence. Additionally, the maxima of bands recorded the in 570–630 nm spectral scope were shifted from 581 (for GC_{1Tb} sample) to

592 nm (for GC_{1Tb1Eu} sample) for an orange band and from 621 (for GC_{1Tb} sample) up to 612 nm (for GC_{1Tb1Eu} sample) for a red band. Indeed, an enhancement of Eu^{3+} emission via Tb^{3+}/Eu^{3+} ET was much more effective for glass-ceramics than for xerogels.

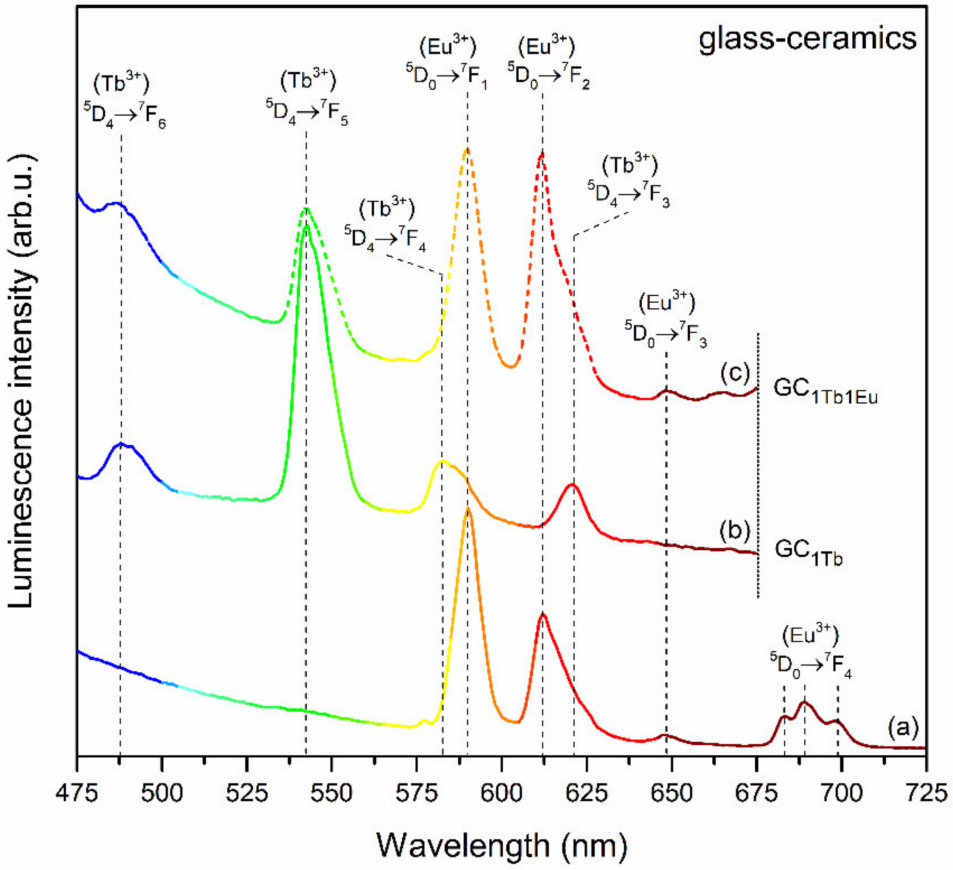

Figure 9. Emission spectra of: (**a**) GC_{1Tb1Eu} (λ_{exc} = 395 nm), (**b**) GC_{1Tb} (λ_{exc} = 351 nm), and (**c**) GC_{1Tb1Eu} (λ_{exc} = 351 nm).

The emission spectra recorded under λ_{exc} = 351 nm for GC_{1TbxEu} co-doped glass-ceramics are depicted in Figure 10. Based on the collected data, it was established that intensities of the $^5D_4 \rightarrow {}^7F_J$ (J = 5,6) bands of Tb^{3+} in the bluish-green spectral scope are strongly dependent on the Tb^{3+}:Eu^{3+} molar ratio. Indeed, the intensity of the Tb^{3+} emission was strongly reduced when the concentration of the acceptor gradually increased, and such an effect was simultaneously accompanied by a well-observable increase in the intensity of Eu^{3+} emission within the reddish-orange spectral scope. The observed correlations in mutual intensities of characteristic emission bands were accompanied by an adequate increase in R/G ratio values from 0.14 (GC_{1Tb}) and 0.80 ($GC_{1Tb0.5Eu}$), through 1.60 (GC_{1Tb1Eu}), 2.47 ($GC_{1Tb1.5Eu}$), and up to 3.76 (GC_{1Tb2Eu}). Therefore, the increment in the calculated R/G ratio values was more dynamic for glass-ceramics than for xerogels, for which only a slight increase was reported when the Tb^{3+}:Eu^{3+} molar ratio decreased. Such a correlation was undoubtedly associated with the decreased interionic distance between Tb^{3+} and Eu^{3+} ions due to their successful entering into the CaF_2 crystal lattice.

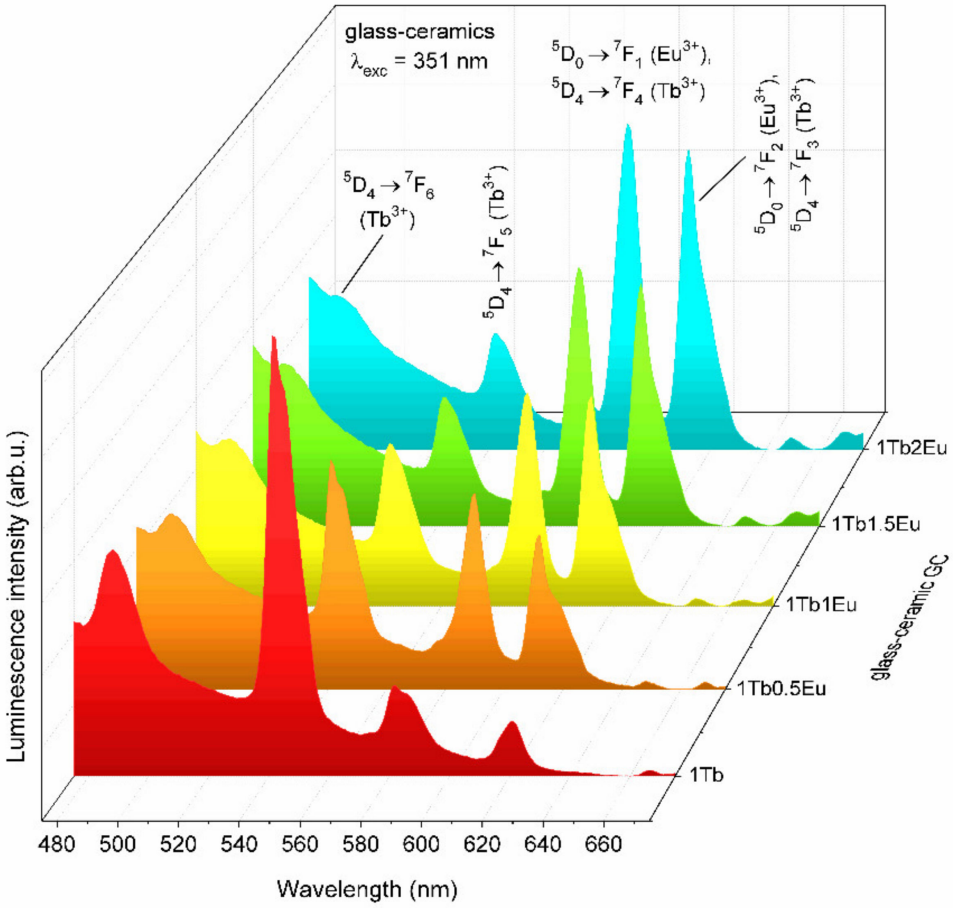

Figure 10. The emission spectra of GC_{1Tb} and GC_{1TbxEu} xerogels recorded under excitation at λ_{exc} = 351 nm.

For Tb^{3+} ions, the G/B ratio analysis defined as $I(^5D_4 \rightarrow {}^7F_5)/I(^5D_4 \rightarrow {}^7F_6)$ could also be treated as a useful tool for characterization of the symmetry around Tb^{3+} dopant ions [65]. Since the $^5D_4 \rightarrow {}^7F_5$ line is a magnetic-dipole in nature and the $^5D_4 \rightarrow {}^7F_6$ transition is an electric-dipole one, the G/B ratio value should have changed when xerogels were transformed into glass-ceramic counterparts. Hence, the G/B ratio values should have been higher in more centrosymmetric sites [66]. Indeed, some changes in emission lines originated from Tb^{3+} ions could also be observed, similarly as for Eu^{3+}. On the other hand, it should be pointed out that the G/B ratio was not as sensitive a spectroscopic probe as the R/O ratio calculated for Eu^{3+} optically active ions. The G/B ratio was calculated for samples singly-doped with Tb^{3+} ions, and the ratio changes from 2.95 (XG_{1Tb}) to 3.80 (GC_{1Tb}). The results were consistent with the data presented by us earlier in our previous work, concentrating on Tb^{3+}-doped sol-gel materials' photoluminescence behavior [67]. Based on structural changes undergone during controlled ceramization at 350 °C, the identified differences in G/B ratio values were clearly related to the migration of Tb^{3+} ions from the amorphous silicate sol-gel network into CaF_2 nanocrystals formed during controlled heat-treatment.

3.2.3. Effect of Changing in the Tb^{3+}:Eu^{3+} Molar Ratio on Decay Times of the $^5D_4$ (Tb^{3+})

The further evaluation of Tb^{3+}/Eu^{3+} ET in fabricated sol-gel materials was based on the decay analysis of the $^5D_4$ excited state of Tb^{3+} ions. Firstly, the interpretation of collected data allowed us to establish a clear correlation between the decay profile (mono- or double-exponential) and type of sol-gel material (i.e., xerogel or glass-ceramic). Indeed, the

curves recorded for xerogels were well-fitted to a first exponential decay mode described by the following equation:

$$I(t) = I_0 \exp(-t/\tau) \quad (3)$$

where I(t) and I_0 are the luminescence intensities at time t and t = 0, respectively, while τ is the luminescence decay time [68]. Factually, in our xerogels, the rare-earths were chemically bonded with OH moieties and CF_3COO^- anions in complex compounds [69]. It should be noted that high vibrational energies characterize such ligands, i.e., >3000 (OH groups) and ~1200, ~1140 cm^{-1} (CF_3COO^- anions) as was demonstrated in the Structural characterization: XRD, TEM, and IR spectroscopy section (Figure 2). According to the energy gap law, the effective phonons with maximum energy located in a local surrounding of RE^{3+} ions ($\hbar\omega_{max}$) generate the strongest effect on decay times [70]. In this case, since OH moieties' vibrational energy was the highest, they played a major role in the non-radiative depopulation of excited states. For glass-ceramics, the decay curves were well-fitted to a second exponential decay mode, which can be expressed by the equation:

$$I(t)/I_0 = A_1 \exp(-t/\tau_1) + A_2 \exp(-t/\tau_2) \quad (4)$$

where A_1 and A_2 are amplitudes, while τ_1 and τ_2 are the decay times of short and long lifetime components, respectively [68]. The double-exponential decay profile, as well as considerable differences in τ_1 and τ_2 values, allowed us to conclude about the distribution of rare-earths between two chemically distinct surroundings characterized by different phonon energies. In fact, part of the RE^{3+} ions migrated during the controlled heat-treatment into the CaF_2 crystal lattice, and formed inside the amorphous sol-gel network as a new chemical environment with low phonon energy (~466 cm^{-1}). Due to such a low phonon energy of the CaF_2 lattice, the multiphonon non-radiative depopulation of excited states was strongly restricted. However, the remainder of rare-earths was located in an amorphous sol-gel host. According to IR-ATR spectra recorded for glass-ceramics (Figure 2), it was observed that an intensity of the broad infrared signal originated from OH moieties was significantly reduced; therefore, a major role in non-radiative relaxation was attributed to Q^3 groups (~1030 cm^{-1}). Nevertheless, their phonon energy was greater than that of CaF_2 crystal lattice. Such differences in phonon energies in the nearest surrounding of rare-earths determined the variable rates of radiative depopulation of their excited states: In silicate sol-gel host, the lifetimes were shorter (τ_1 components), while in the CaF_2 crystal lattice, the lifetimes were prolonged (τ_2 components). Based on such distinguished lifetime components and their relative contributions to the total radiative decay profile, the average luminescence lifetime could be calculated using the following formula [71]:

$$\tau_{avg} = \frac{A_1\tau_1^2 + A_2\tau_2^2}{A_1\tau_1 + A_2\tau_2} \quad (5)$$

The luminescence decay curves of the $^5D_4$ state (Tb^{3+}) recorded for XG_{1Tb}, GC_{1Tb}, as well as for individual XG_{1TbxEu}, GC_{1TbxEu} co-doped sol-gel samples are measured and plotted in Figures 11 and 12, respectively. The decay curves were recorded upon λ_{exc} = 351 nm excitation and monitoring λ_{em} = 541 nm green luminescence of Tb^{3+} ions. A slight shortening of the decay lifetime was observed for xerogels from 1.18 (XG_{1Tb}) to 1.04, 1.01, 0.96, and 0.91 ms for $XG_{1Tb0.5Eu}$, XG_{1Tb1Eu}, $XG_{1Tb1.5Eu}$, and XG_{1Tb2Eu}, respectively. For glass-ceramics, a change in the Tb^{3+}:Eu^{3+} molar ratio from 1:0.5 to 1:2 resulted in significantly more efficient shortening of the average decay time of the $^5D_4$ state from 4.75 (GC_{1Tb}) to 3.75 ($GC_{1Tb0.5Eu}$), 2.59 (GC_{1Tb1Eu}), 1.92 ($GC_{1Tb1.5Eu}$), and 1.55 ms (GC_{1Tb2Eu}) (the individual values of τ_1 and τ_2 components are depicted in Tables 1 and 2). Shorter luminescence lifetimes for xerogels than for glass-ceramics (when we compare the samples with the same Tb^{3+}:Eu^{3+} molar ratio) were caused by the coordination of Tb^{3+} ions by high-vibrational OH groups, involved in the non-radiative depopulation of the $^5D_4$ level. Their remarkable removal during controlled heat-treatment and partial segregation of Tb^{3+} inside CaF_2 nanocrystals with low-phonon energy allowed the share of non-radiative

processes in relaxation to be reduced significantly; hence, the lifetimes from the $^5D_4$ state for glass-ceramics were longer.

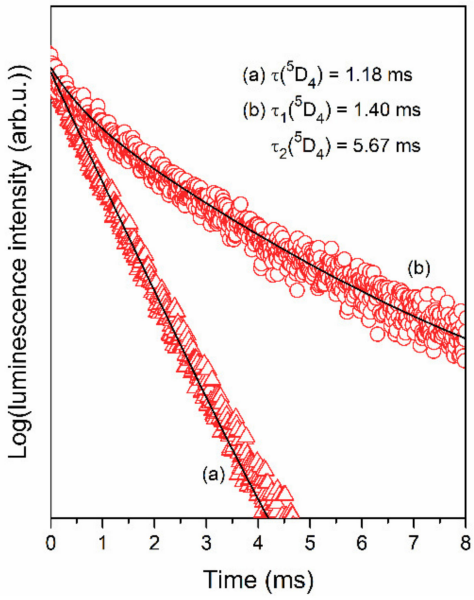

Figure 11. Luminescence decay curves of the $^5D_4$ level of Tb^{3+} ions recorded for (**a**) XG_{1Tb}, and (**b**) GC_{1Tb}.

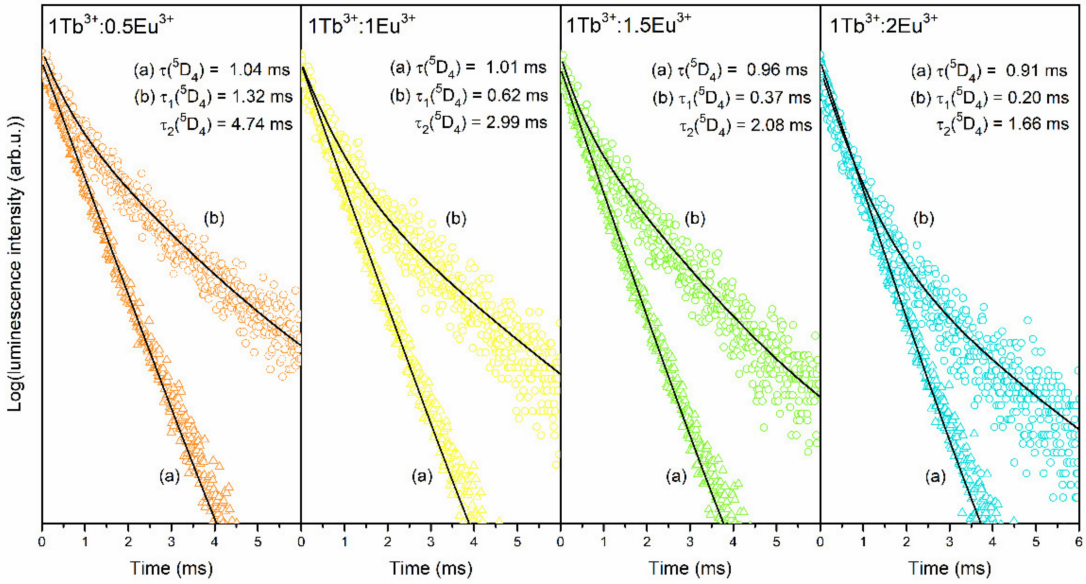

Figure 12. Luminescence decay curves of the $^5D_4$ (Tb^{3+}) level recorded for individual XG_{1TbxEu} and GC_{1TbxEu} co-doped samples: (**a**) Xerogels, (**b**) glass-ceramics. The curves were recorded upon excitation at λ_{exc} = 351 nm.

Table 1. Measured lifetimes of the $^5D_4$ state (Tb^{3+}), energy transfer efficiencies, and R/G ratio values for prepared xerogels.

Xerogel	$\tau(^5D_4)$ (ms)	η_{ET} (%)	R/G
XG_{1Tb}	1.18	-	0.09
$XG_{1Tb0.5Eu}$	1.04	11.9	0.15
XG_{1Tb1Eu}	1.01	14.4	0.17
$XG_{1Tb1.5Eu}$	0.96	18.6	0.26
XG_{1Tb2Eu}	0.91	22.9	0.30

Table 2. Measured lifetimes of the $^5D_4$ state (Tb^{3+}), average decay times, energy transfer efficiencies, and R/G ratio values for prepared glass-ceramics.

Glass-Ceramic	$\tau_m(^5D_4)$ (ms)	$\tau_{avg}(^5D_4)$ (ms)	η_{ET} (%)	R/G
GC_{1Tb}	1.40 (τ_1) 5.67 (τ_2)	4.75	-	0.14
$GC_{1Tb0.5Eu}$	1.32 (τ_1) 4.74 (τ_2)	3.75	25.7	0.80
GC_{1Tb1Eu}	0.62 (τ_1) 2.99 (τ_2)	2.59	45.5	1.60
$GC_{1Tb1.5Eu}$	0.37 (τ_1) 2.08 (τ_2)	1.92	59.6	2.47
GC_{1Tb2Eu}	0.20 (τ_1) 1.66 (τ_2)	1.55	67.4	3.76

Since the shortening in luminescence lifetimes was caused by an energy transfer from Tb^{3+} towards Eu^{3+} ions, the ratio of luminescence lifetimes of the $^5D_4$ state of Tb^{3+} ions in the presence (τ) and the absence of Eu^{3+} ions (τ_0) could be used as a valuable tool to estimate the energy transfer efficiency [72]:

$$\eta_{ET} = \left(1 - \frac{\tau}{\tau_0}\right) \times 100\% \quad (6)$$

For xerogels, the η_{ET} values increased from 11.86% ($XG_{1Tb0.5Eu}$) through 14.41% (XG_{1Tb1Eu}), 18.64% ($XG_{1Tb1.5Eu}$) to 22.88% (XG_{1Tb2Eu}). Compared to xerogels, a prompt increase in η_{ET} values has been noted for glass-ceramic materials, which reached 25.69% ($GC_{1Tb0.5Eu}$), 45.47% (GC_{1Tb1Eu}), 59.58% ($GC_{1Tb1.5Eu}$), and 67.37% (GC_{1Tb2Eu}). Hence, it was easily observed that the energy transfer efficiencies estimated for glass-ceramic samples were noticeably higher than for analogous xerogels with the same Tb^{3+}:Eu^{3+} molar ratio, which was mainly caused by migration of rare-earths into the CaF_2 crystal lattice during controlled heat-treatment, where the interionic Tb^{3+}–Eu^{3+} distances were significantly shorter than in the amorphous sol-gel host. Additionally, those results clearly indicated a correlation between η_{ET} and a change in the Tb^{3+}:Eu^{3+} molar ratio from 1:0.5 to 1:2 in fabricated sol-gel materials, which was undoubtedly associated with a higher probability that more Eu^{3+} ions could be located adjacent to Tb^{3+}. Indeed, since the Tb^{3+}/Eu^{3+} ET is characterized by dipole-dipole interactions [13,16], ET's probability is proportional to $1/R^6$ (R is the average distance between Tb^{3+} and Eu^{3+}). On this occasion, when Tb^{3+} and Eu^{3+} dopants were segregated inside CaF_2 nanocrystal lattice, the interionic distances of Tb^{3+}–Eu^{3+} pairs were vastly shortened notably if the Tb^{3+}:Eu^{3+} molar ratio changed (from 1:0.5 to 1:2).

For better readability, the correlation between the R/G ratio, η_{ET}, and $\tau(^5D_4)$ lifetimes for prepared sol-gel samples are graphically presented in Figure 13 and depicted in Table 1 (for xerogels) and Table 2 (for glass-ceramics). The R/G ratio gradually increased when the Tb^{3+}:Eu^{3+} molar ratio changed from 1:0.5 to 1:2, pointing to the increasing share of emissions originated from Eu^{3+} ions, along with gradual growth in η_{ET} values and shortening of the $\tau(^5D_4)$ decay times of Tb^{3+} ions. For xerogels and glass-ceramic materials, such a relation was due to the increasing content of Eu^{3+} ions in accordance with Tb^{3+}. The changes in the values of the parameters mentioned above for glass-ceramics materials were much more significant for each change of the Tb^{3+}:Eu^{3+} molar ratio, which resulted from the preferential segregation of optically active ions into the CaF_2 nanophase.

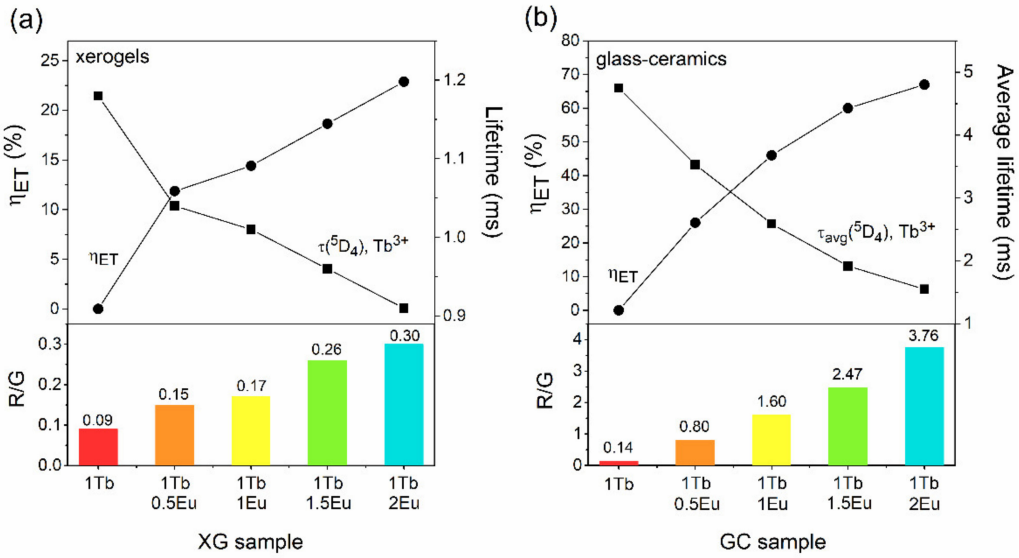

Figure 13. The relation between R/G ratio, energy transfer efficiency (η_{ET}), and lifetime of the $^5D_4$ (Tb^{3+}) state for: xerogels (**a**) and glass-ceramics (**b**).

3.2.4. The Luminescence Decay Analysis of the $^5D_0$ State of Eu^{3+} Ions

The characterization of luminescence properties of fabricated Tb^{3+}/Eu^{3+} co-doped sol-gel materials was supplemented by decay analysis of the $^5D_0$ level (Eu^{3+}) upon excitation at λ_{exc} = 394 wavelength and monitoring λ_{em} = 592 nm (Figure 14). The decay times were also depicted in Table 3 (for xerogels) and Table 4 (for glass-ceramics).

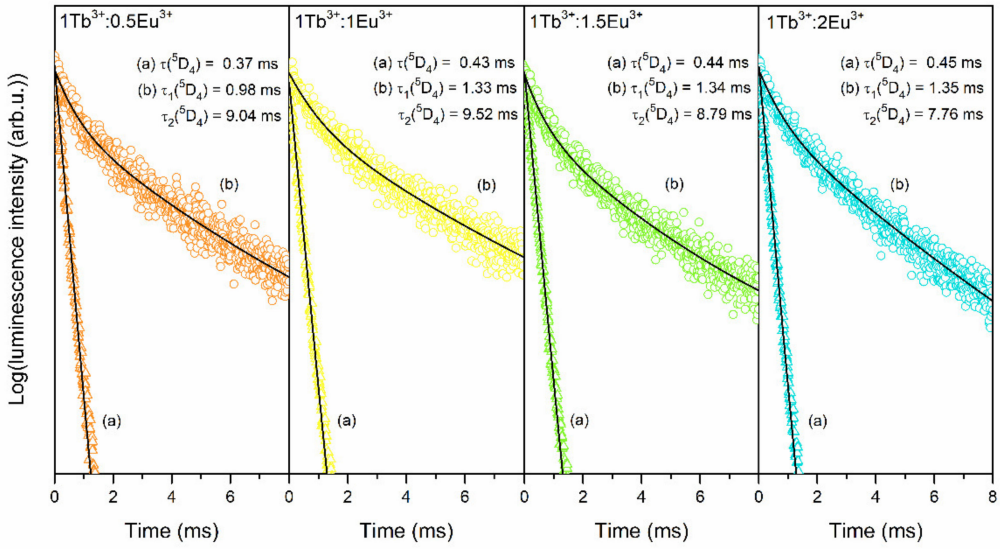

Figure 14. Luminescence decay curves of the $^5D_0$ state of Eu^{3+} ions recorded for: (**a**) xerogels (λ_{exc} = 395) and (**b**) glass-ceramics (λ_{exc} = 394 nm).

Table 3. Measured lifetimes of the $^5D_0$ state (Eu^{3+}) in xerogels (λ_{exc} = 395 nm excitation).

Xerogel	$\tau(^5D_0)$ (ms)
$XG_{1Tb0.5Eu}$	0.37
XG_{1Tb1Eu}	0.43
$XG_{1Tb1.5Eu}$	0.44
XG_{1Tb2Eu}	0.45

Table 4. Measured lifetimes and calculated average decay times of the $^5D_0$ state (Eu^{3+}) in fabricated glass-ceramics (λ_{exc} = 394 nm excitation).

Glass-Ceramic	λ_{exc} = 394 nm	
	$\tau_m(^5D_0)$ (ms)	$\tau_{avg}(^5D_0)$ (ms)
$GC_{1Tb0.5Eu}$	0.98 (τ_1) 9.04 (τ_2)	8.40
GC_{1Tb1Eu}	1.33 (τ_1) 9.52 (τ_2)	8.59
$GC_{1Tb1.5Eu}$	1.34 (τ_1) 8.79 (τ_2)	7.94
GC_{1Tb2Eu}	1.35 (τ_1) 7.76 (τ_2)	6.96

For xerogels, the $\tau(^5D_0)$ lifetime values hesitated from 0.37 ($XG_{1Tb0.5Eu}$), 0.43 (XG_{1Tb1Eu}), 0.44 ($XG_{1Tb1.5Eu}$), to 0.45 ms (XG_{1Tb2Eu}). The growing content of Eu^{3+} caused such a slight increase in decay times in prepared xerogels due to changing the Tb^{3+}:Eu^{3+} molar ratio from 1:0.5 to 1:2. The relatively short luminescence lifetimes were caused by numerous OH groups in the immediate vicinity of Eu^{3+} ions in the silicate xerogel host. Interestingly, it was found that the $\tau_{avg}(^5D_0)$ lifetimes in glass-ceramics exhibited no evident and straightforward correlation with the increasing content of Eu^{3+} ions as was found for xerogels. Indeed, the partial segregation of optically active dopants in CaF_2 nanocrystals was responsible for the effective shortening of average distances between them and may have caused competition between radiative and non-radiative processes. Comparing the individual $\tau_{avg}(^5D_0)$ lifetime values when the λ_{exc} = 394 nm wavelength was used as an excitation source, it was easy to observe that changing the Tb^{3+}:Eu^{3+} molar ratio from 1:0.5 to 1:1 promoted the slight lifetime prolongation ($\tau_{avg}(^5D_0)$ = 8.40 for $GC_{1Tb0.5Eu}$ and $\tau_{avg}(^5D_0)$ = 8.59 ms for GC_{1Tb1Eu}). Meanwhile, a further change in the Tb^{3+}:Eu^{3+} molar ratio (1:1.5 and 1:2) caused shortening of the calculated average decay time ($\tau_{avg}(^5D_0)$ = 7.94 for $GC_{1Tb1.5Eu}$ and $\tau_{avg}(^5D_0)$ = 6.96 ms for GC_{1Tb2Eu}). Since the R/O ratio values were almost the same for all fabricated glass-ceramic samples (from 0.59 to 0.64), we could assume that the relative distribution of Eu^{3+} ions between CaF_2 nanocrystals and the amorphous sol-gel host was comparable in any case. Simultaneously, it also meant that the content of Eu^{3+} ions in precipitated CaF_2 nanocrystals should have been proportional to the total concentration of Eu^{3+} introduced during the performed synthesis. Such a relation of the decrease in $\tau_{avg}(^5D_0)$ values, when the Tb^{3+}:Eu^{3+} molar ratio equaled 1:1.5 and 1:2, could be explained by the cross-relaxation process. In this case, an excited Eu^{3+} ion made a downward transition ($^5D_2 \rightarrow {}^5D_1$ and/or $^5D_1 \rightarrow {}^5D_0$), whereas a coupled unexcited neighboring Eu^{3+} ion made an upward transition ($^7F_0 \rightarrow {}^7F_4$ and/or $^7F_0 \rightarrow {}^7F_3$) [73]. Such non-radiative relaxation depended on the separation between Eu^{3+} interacting ions; hence, the shortening in the interionic distance inside CaF_2 nanocrystals (promoted when the Tb^{3+}:Eu^{3+} molar ratio exceeds 1:1) would be predominantly responsible for such a decrease in $\tau_{avg}(^5D_0)$. To compare, in the case of Tb^{3+} ions, we excluded an involvement of the cross-relaxation process on luminescence lifetimes of the $^5D_4$ state based on our previous results for SiO_2-PbF_2:Tb^{3+} sol-gel glass-ceramics, for which we reported the non-radiative relaxation mechanism when the molar ratio of Tb^{3+} (in accordance to Pb^{2+} cations) exceeded 0.6:1 [67]. On the other hand, since fabricated sol-gel samples were Eu^{3+} low-concentrated, such shortening of the $\tau_{avg}(^5D_0)$ decay times when the Tb^{3+}:Eu^{3+} molar ratio equaled 1:1.5 and 1:2 could be caused by lattice defects, which are well-known as quenching channels [74]. Indeed, a charge compensation induced the formation of vacancies inside the crystal lattice, the number of which would be greater if greater amounts of trivalent dopant ions entered into CaF_2 nanocrystals [75]. Hence, the defects could be responsible for effective faster depopulation of the $^5D_0$ state when the content of Eu^{3+} grows, resulting in shortening of the $\tau_{avg}(^5D_0)$ decay times. Moreover, it is interesting to note that

the $\tau_{avg}(^5D_0)$ lifetime was prolonged when the Tb^{3+}:Eu^{3+} molar ratio was achieved 1:1, and then reduced when the molar ratio equaled to 1:1.5 and 1:2, whereas the luminescence intensity was still increased. A similar effect was also observed for Eu^{3+}-doped silicate hybrid materials [76]. The luminescence intensity successfully grew from 0.1 mol% up to 1 mol%; however, it was reported that the lifetimes of the $^5D_0$ state gradually reduced from 617 (for 0.1 mol% Eu^{3+}-doped sample) to 275 µs (for 1 mol% Eu^{3+}-doped sample). In the case of our fabricated sol-gel samples, the experimental results from luminescence decay analysis have clearly proven that the variable molar ratio of Tb^{3+}:Eu^{3+} and controlled crystallization of amorphous xerogels could be responsible for modulating the character of interionic processes.

Based on recorded emission spectra and performed decay analysis of the $^5D_0$ state of Eu^{3+} ions, the quantum yields, Φ_{Eu}, were calculated using $\Phi = k_R/k$ equation. In this equation, k is the total decay rate constant ($k = 1/\tau(^5D_0)$), whereas k_R is the radiative rate constant. The value of k_R was estimated from the following relation [77]:

$$k_R = A_{MD,0} n^3 \left(\frac{I_{tot}}{I_{MD}} \right) \quad (7)$$

where I_{tot} is the sum of integrated intensities of the $^5D_0 \rightarrow {}^7F_J$ (J = 0–4) emission bands of Eu^{3+}, I_{MD} is the integrated intensity of the $^5D_0 \rightarrow {}^7F_1$ magnetic-dipole transition, n is the refractive index of the host and $A_{MD,0}$ denotes the Einstein spontaneous emission coefficient for the $^5D_0 \rightarrow {}^7F_1$ transition and its value for sol-gel systems is equal to 14.65 s^{-1} [78]. Similar to previous reports for CaF_2 thin films [79] and CaF_2 nanoparticles produced by the fluorolytic sol-gel process [80], the refractive index of CaF_2 nanocrystals was close to n = 1.44. The quantum efficiencies for xerogels were very similar and hesitated from 9.3% to 10.5%. These values were changed drastically during controlled heat-treatment when xerogels were transformed into glass-ceramic systems. The quantum efficiencies achieved the following values: 75.6% ($GC_{1Tb0.5Eu}$), 76.1% (GC_{1Tb1Eu}), 69.0% ($GC_{1Tb1.5Eu}$), and 60.0% (GC_{1Tb2Eu}). Our calculations are in good agreement with results reported by Sun et al. [81] for Eu^{3+}-doped CaF_2 thin films, for which the highest quantum efficiency was estimated to 64.24%.

4. Conclusions

In summary, the Tb^{3+}/Eu^{3+} ET was systematically investigated in a series of xerogels and glass-ceramics containing CaF_2 nanocrystals and the variable Tb^{3+}:Eu^{3+} molar ratio. The transformation of amorphous xerogels into glass-ceramics was successfully carried out at as low a temperature as 350 °C. A particular emphasis was placed on determining the correlation between the photoluminescence properties of prepared sol-gel materials and controlled crystallization, as well as the change in the Tb^{3+}:Eu^{3+} molar ratio. The following points have been established:

- Using spectroscopy of Eu^{3+} ions as spectral probes, it was found that optically active dopants were preferably segregated inside the lattice of CaF_2 nanocrystals during controlled heat-treatment of initial xerogels. Indeed, the $^5D_0 \rightarrow {}^7F_1$ MD transition occupied the predominant advantage for glass-ceramics, which resulted in an almost six-fold decline in R/O ratio values from approximately 3.70 (for amorphous xerogels) to 0.64 (reported after controlled ceramization);
- The growing R/G ratio (from 0.09 to 0.30 for xerogels, and from 0.14 to 3.76 for glass-ceramics) was observed when the Tb^{3+}:Eu^{3+} molar ratio changed from 1:0.5 to 1:2. Notably, in glass-ceramics, the emission of Tb^{3+} ions visibly gradually weakened, while luminescence of Eu^{3+} ions occupied the predominant advantage, significantly enhancing the reddish-orange emission;
- Performed decay analysis revealed an interesting dependence of decay times on change in the Tb^{3+}:Eu^{3+} molar ratio, as well as partial segregation of Tb^{3+} and Eu^{3+} ions inside CaF_2 nanocrystals formed during controlled heat-treatment at 350 °C.

Indeed, a well-observable gradual shortening in $\tau(^5D_4)$ lifetimes for Tb^{3+} ions when the Tb^{3+}:Eu^{3+} molar ratio changed from 1:0.5 to 1:2 was reported for xerogels (from 1.18 to 0.91 ms) and glass-ceramics (from 4.75 to 1.55 ms), and it was accompanied by an adequate increase in η_{ET} (from 11.9% to 22.9% for xerogels and from 25.7% to 67.4% for glass-ceramics). Higher η_{ET} values for the glass-ceramics resulted from a significant reduction in interionic distances between Tb^{3+} and Eu^{3+} ions inside the CaF_2 crystal lattice;

- The decay analysis of the $^5D_0$ state (Eu^{3+}) clearly revealed that the partial crystallization induced a remarkable prolongation of $\tau_{avg}(^5D_0)$ lifetimes even to 8.59 ms when the Tb^{3+}:Eu^{3+} molar ratio equals 1:1, however, the further change in Tb^{3+}:Eu^{3+} caused a slight shortening of decay times (7.94 when Tb^{3+}:Eu^{3+} = 1:1.5, and 6.96 ms when Tb^{3+}:Eu^{3+} = 1:2), which indicated a competition between radiative and non-radiative processes.

Author Contributions: Conceptualization, N.P.; methodology, N.P. and B.S.-S.; software, N.P.; validation, N.P.; formal analysis, N.P.; investigation, N.P., T.G., and J.P.; resources, W.A.P.; data curation, N.P.; writing—original draft preparation, N.P.; writing—review and editing, W.A.P.; visualization, N.P.; supervision, N.P.; project administration, N.P.; funding acquisition, W.A.P. All authors have read and agreed to the published version of the manuscript.

Funding: This research was funded by National Science Centre (Poland), grant number 2016/23/B/ST8/01965.

Data Availability Statement: The data presented in this study are available on request from the corresponding author.

Conflicts of Interest: The authors declare no conflict of interest.

References

1. Fischer, S.; Pier, T.; Jüstel, T. On the sensitization of Eu^{3+} with Ce^{3+} and Tb^{3+} by composite structured $Ca_2LuHf_2Al_3O_{12}$ garnet phosphors for blue LED excitation. *Dalton Trans.* **2019**, *48*, 315–323. [CrossRef] [PubMed]
2. Psuja, P.; Hreniak, D.; Strek, W. Rare-Earth Doped Nanocrystalline Phosphors for Field Emission Displays. *J. Nanomater.* **2007**. [CrossRef]
3. Kränkel, C.; Marzahl, D.-T.; Moglia, F.; Huber, G.; Metz, P.W. Out of the blue: Semiconductor laser pumped visible rare-earth doped lasers. *Laser Photonics Rev.* **2016**, *10*, 548–568. [CrossRef]
4. Klier, D.T.; Kumke, M.U. Upconversion $NaYF_4$:Yb:Er nanoparticles co-doped with Gd^{3+} and Nd^{3+} for thermometry on the nanoscale. *RSC Adv.* **2015**, *5*, 67149–67156. [CrossRef]
5. Han, L.; Song, J.; Liu, W.; Xiao, A.; Zhang, L.; Lu, A.; Xiao, Z.; You, W.; Zhang, Q. Preparation and luminescent properties of Tm^{3+}-Dy^{3+} co-doped phosphate glass for white light-emitting-diode applications. *J. Lumin.* **2020**, *227*, 117559. [CrossRef]
6. Bian, W.; Lin, Y.; Wang, T.; Yu, X.; Qiu, J.; Zhou, M.; Luo, H.; Yu, S.F.; Xu, X. Direct Identification of Surface Defects and Their Influence on the Optical Characteristics of Upconversion Nanoparticles. *ACS Nano* **2018**, *12*, 3623–3628. [CrossRef]
7. Boyer, J.-C.; Cuccia, L.A.; Capobianco, J.A. Synthesis of Colloidal Upconverting $NaYF_4$:Er^{3+}/Yb^{3+} and Tm^{3+}/Yb^{3+} Monodisperse Nanocrystals. *Nano Lett.* **2007**, *7*, 847–852. [CrossRef]
8. Saidi, K.; Dammak, M. Crystal structure, optical spectroscopy and energy transfer properties in $NaZnPO_4$:Ce^{3+},Tb^{3+} phosphors for UV-based LEDs. *RSC Adv.* **2020**, *10*, 21867–21875. [CrossRef]
9. Xu, C.; Guan, H.; Song, Y.; An, Z.; Zhang, X.; Zhou, X.; Shi, Z.; Sheng, Y.; Zou, Y.H. Novel highly efficient single-component multi-peak emitting aluminosilicate phosphors co-activated with Ce^{3+},Tb^{3+} and Eu^{2+}: Luminescence properties, tunable color, and thermal properties. *Phys. Chem. Chem. Phys.* **2018**, *20*, 1591–1607. [CrossRef]
10. Wang, T.; Yu, H.; Siu, C.K.; Qiu, J.; Xu, X.; Yu, S.F. White-light whispering-gallery-mode lasing from lanthanide-doped upconversion $NaYF_4$ hexagonal microrods. *ACS Photonics* **2017**, *4*, 1539–1543. [CrossRef]
11. Hassairi, M.A.; Dammak, M.; Zambou, D.; Chadeyron, G.; Mahiou, R. Red-green-blue upconversion luminescence and energy transfer in Yb^{3+}/Er^{3+}/Tm^{3+} doped YP_5O_{14} ultraphosphates. *J. Lumin.* **2017**, *181*, 393–399. [CrossRef]
12. Chu, Y.; Ren, J.; Zhang, J.; Peng, G.; Yang, J.; Wang, P.; Yuan, L. Ce^{3+}/Yb^{3+}/Er^{3+} triply doped bismuth borosilicate glass: A potential fiber material for broadband near-infrared fiber amplifiers. *Sci. Rep.* **2016**, *6*, 33865. [CrossRef]
13. Li, B.; Huang, X.; Guo, H.; Zeng, Y. Energy transfer and tunable photoluminescence of $LaBWO_6$:Tb^{3+}, Eu^{3+} phosphors for near-UV white LEDs. *Dyes Pigm.* **2018**, *150*, 67–72. [CrossRef]
14. Baur, F.; Glocker, F.; Jüstel, T. Photoluminescence and energy transfer rates and efficiencies in Eu^{3+} activated $Tb_2Mo_3O_{12}$. *J. Mater. Chem. C* **2015**, *3*, 2054–2064. [CrossRef]

15. Mi, R.; Chen, J.; Liu, Y.-G.; Fang, M.; Mei, L.; Huang, Z.; Wang, B.; Zhaob, C. Luminescence and energy transfer of a color tunable phosphor: Tb^{3+} and Eu^{3+} co-doped $ScPO_4$. *RSC Adv.* **2016**, *6*, 28887–28894. [CrossRef]
16. Xu, M.; Ding, Y.; Luo, W.; Wang, L.; Li, S.; Liu, Y. Synthesis, luminescence properties and energy transfer behavior of color-tunable $KAlP_2O_7$:Tb^{3+}, Eu^{3+} phosphors. *Opt. Laser Technol.* **2020**, *121*, 105829. [CrossRef]
17. Xia, Y.; Zou, X.; Zhang, H.; Zhao, M.; Chen, X.; Jia, W.; Su, C.; Shao, J. Luminescence and energy transfer studies of Eu^{3+}-Tb^{3+} co-doped transparent glass ceramics containing $BaMoO_4$ crystallites. *J. Alloys Compd.* **2019**, *774*, 540–546. [CrossRef]
18. Yao, L.-Q.; Chen, G.-H.; Yang, T.; Cui, S.-C.; Li, Z.-C.; Yang, Y. Energy transfer, tunable emission and optical thermometry in Tb^{3+}/Eu^{3+} co-doped transparent $NaCaPO_4$ glass ceramics. *Ceram. Int.* **2016**, *42*, 13086–13090. [CrossRef]
19. Chen, D.; Wang, Z.; Zhou, Y.; Huang, P.; Ji, Z. Tb^{3+}/Eu^{3+}: YF_3 nanophase embedded glass ceramics: Structural characterization, tunable luminescence and temperature sensing behavior. *J. Alloys Compd.* **2015**, *646*, 339–344. [CrossRef]
20. Kłonkowski, A.M.; Wiczk, W.; Ryl, J.; Szczodrowski, K.; Wileńska, D. A white phosphor based on oxyfluoride nano-glass-ceramics co-doped with Eu^{3+} and Tb^{3+}: Energy transfer study. *J. Alloys Compd.* **2017**, *724*, 649–653. [CrossRef]
21. Hu, F.; Zhao, Z.; Chi, F.; Wei, X.; Yin, M. Structural characterization and temperature-dependent luminescence of CaF_2:Tb^{3+}/Eu^{3+} glass ceramics. *J. Rare Earth.* **2017**, *35*, 536–541. [CrossRef]
22. Li, X.; Peng, Y.; Wei, X.; Yuan, S.; Zhu, Y.; Chen, D. Energy transfer behaviors and tunable luminescence in Tb^{3+}/Eu^{3+} codoped oxyfluoride glass ceramics containing cubic/hexagonal $NaYF_4$ nanocrystals. *J. Lumin.* **2019**, *210*, 182–188. [CrossRef]
23. Li, X.; Chen, X.; Yuan, S.; Liu, S.; Wang, C.; Chen, D. Eu^{3+}-Doped glass ceramics containing $NaTbF_4$ nanocrystals: Controllable glass crystallization, Tb^{3+}-bridged energy transfer and tunable luminescence. *J. Mater. Chem. C* **2017**, *3*, 10201–10210. [CrossRef]
24. Xu, F.; Wei, X.; Jiang, S.; Huang, S.; Qin, Y.; Chen, Y.; Duan, C.-K.; Yin, M. Fabrication and Luminescence Properties of Transparent Glass-Ceramics Containing Eu^{3+}-Doped $TbPO_4$ Nanocrystals. *J. Am. Ceram. Soc.* **2015**, *98*, 464–468. [CrossRef]
25. Wang, R.; Zhou, D.; Qiu, J.; Yang, Y.; Wang, C. Color-tunable luminescence in Eu^{3+}/Tb^{3+} co-doped oxyfluoride glass and transparent glass-ceramics. *J. Alloys Compd.* **2015**, *629*, 310–314. [CrossRef]
26. Koseva, I.; Tzvetkov, P.; Ivanov, P.; Yordanova, A.; Nikolov, V. Terbium and europium co-doped $NaAlSiO_4$ nano glass-ceramics for LED application. *Optik* **2017**, *137*, 45–50. [CrossRef]
27. Gorni, G.; Velázquez, J.J.; Mosa, J.; Balda, R.; Fernández, J.; Durán, A.; Castro, Y. Transparent glass-ceramics produced by sol-gel: A suitable alternative for photonic materials. *Materials* **2018**, *11*, 212. [CrossRef]
28. Velázquez, J.J.; Mosa, J.; Gorni, G.; Balda, R.; Fernández, J.; Durán, A.; Castro, Y. Novel sol-gel SiO_2-$NaGdF_4$ transparent nano-glass-ceramics. *J. Non Cryst. Solids* **2019**, *520*, 119447. [CrossRef]
29. Gorni, G.; Velázquez, J.J.; Mosa, J.; Mather, G.C.; Serrano, A.; Vila, M.; Castro, G.R.; Bravo, D.; Balda, R.; Fernández, J.; et al. Transparent sol-gel oxyfluoride glass-ceramics with high crystalline fraction and study of RE incorporation. *Nanomaterials* **2019**, *9*, 530. [CrossRef]
30. Danks, A.E.; Hall, S.R.; Schnepp, Z. The evolution of 'sol-gel' chemistry as a technique for materials synthesis. *Mater. Horiz.* **2016**, *3*, 91–112. [CrossRef]
31. Carta, D.; Pickup, D.M.; Knowles, J.C.; Ahmed, I.; Smith, M.E.; Newport, R.J. A structural study of sol–gel and melt-quenched phosphate-based glasses. *J. Non Cryst. Solids* **2007**, *353*, 1759–1765. [CrossRef]
32. Wang, H.; Ye, S.; Liu, T.; Li, S.; Hu, R.; Wang, D. Influence of local phonon energy on quantum efficiency of Tb^{3+}-Yb^{3+} co-doped glass ceramics containing fluoride nanocrystals. *J. Rare Earth.* **2014**, *33*, 201–205. [CrossRef]
33. Deng, W.; Cheng, J.-S. New transparent glass-ceramics containing large grain Eu^{3+}: CaF_2 nanocrystals. *Mater. Lett.* **2012**, *73*, 112–114. [CrossRef]
34. Ryskin, A.I.; Fedorov, P.P.; Bagraev, N.T.; Lushchik, A.; Vasil'chenko, E.; Angervaks, A.E.; Kudryavtseva, I. Stabilization of high-temperature-disorder of fluorine sublattice by quenching in calcium fluoride crystals. *J. Fluor. Chem.* **2017**, *200*, 109–114. [CrossRef]
35. Liu, X.; Li, Y.; Aidilibike, T.; Guo, J.; Di, W.; Qin, W. Pure red upconversion emission from CaF_2:Yb^{3+}/Eu^{3+}. *J. Lumin.* **2017**, *185*, 247–250. [CrossRef]
36. Kuznetsov, S.V.; Morozov, O.A.; Gorieva, V.G.; Mayakova, M.N.; Marisov, M.A.; Voronov, V.V.; Yapryntsev, A.D.; Ivanov, V.K.; Nizamutdinov, A.S.; Semashko, V.V.; et al. Synthesis and luminescence studies of CaF_2:Yb:Pr solid solutions powders for photonics. *J. Fluor. Chem.* **2018**, *211*, 70–75. [CrossRef]
37. Adusumalli, V.N.K.B.; Koppisetti, H.V.S.R.M.; Mahalingam, V. Ce^{3+} sensitized bright white light emission from colloidal Ln^{3+} doped CaF_2 nanocrystals for the development of transparent nanocomposites. *J. Mater. Chem. C* **2016**, *4*, 2289–2294. [CrossRef]
38. Akchurin, M.S.; Basiev, T.T.; Demidenko, A.A.; Doroshenko, M.E.; Fedorov, P.P.; Garibin, E.A.; Gusev, P.E.; Kuznetsov, S.V.; Krutov, M.A.; Mironov, I.A.; et al. CaF_2:Yb laser ceramics. *Opt. Mater.* **2013**, *35*, 444–450. [CrossRef]
39. Liu, G.; Sun, Z.; Fu, Z.; Ma, L.; Wang, X. Temperature sensing and bio-imaging applications based on polyethylene/CaF_2 nanoparticles with upconversion fluorescence. *Talanta* **2017**, *169*, 181–188. [CrossRef] [PubMed]
40. Cheng, Y.; Wang, Y.; Teng, F.; Dong, H.; Chen, L.; Mu, J.; Sun, Q.; Fan, J.; Hu, X.; Miao, H. Down-conversion emission of Ce^{3+}-Tb^{3+} co-doped CaF_2 hollow spheres and application for solar cells. *Mater. Res. Express* **2018**, *5*, 036206. [CrossRef]
41. Pawlik, N.; Szpikowska-Sroka, B.; Goryczka, T.; Pisarski, W.A. Sol-Gel Glass-Ceramic Materials Containing CaF_2:Eu^{3+} Fluoride Nanocrystals for Reddish-Orange Photoluminescence Applications. *Appl. Sci.* **2019**, *9*, 5490. [CrossRef]
42. Pawlik, N.; Szpikowska-Sroka, B.; Goryczka, T.; Pisarski, W.A. Photoluminescence investigation of sol-gel glass-ceramic materials containing SrF_2:Eu^{3+} nanocrystals. *J. Alloys Compd.* **2019**, *810*, 151935. [CrossRef]

43. Pawlik, N.; Szpikowska-Sroka, B.; Pisarska, J.; Goryczka, T.; Pisarski, W.A. Reddish-Orange Luminescence from BaF_2:Eu^{3+} Fluoride Nanocrystals Dispersed in Sol-Gel Materials. *Materials* **2019**, *12*, 3735. [CrossRef] [PubMed]
44. Pawlik, N.; Szpikowska-Sroka, B.; Pisarski, W.A. Energy Transfer Study on Tb^{3+}/Eu^{3+} Co-Activated Sol-Gel Glass-Ceramic Materials Containing MF_3 (M = Y, La) Nanocrystals for NUV Optoelectronic Devices. *Materials* **2020**, *13*, 2522. [CrossRef]
45. Yanes, A.C.; del-Castillo, J.; Ortiz, E. Energy transfer and tunable emission in $BaGdF_5$:RE^{3+} (RE = Ce, Tb, Eu) nano-glass-ceramics. *J. Alloys Compd.* **2019**, *773*, 1099–1107. [CrossRef]
46. Pawlik, N.; Szpikowska-Sroka, B.; Goryczka, T.; Pisarski, W.A. Spectroscopic Properties of Eu^{3+} Ions in Sol-Gel Materials Containing Calcium Fluoride Nanocrystals. *Phys. Status Solidi B* **2019**, *257*, 1900478. [CrossRef]
47. Pawlik, N.; Szpikowska-Sroka, B.; Pietrasik, E.; Goryczka, T.; Pisarski, W.A. Structural and luminescence properties of silica powders and transparent glass-ceramics containing LaF_3:Eu^{3+} nanocrystals. *J. Am. Ceram. Soc.* **2018**, *101*, 4654–4668. [CrossRef]
48. Holder, C.F.; Schaak, R.E. Tutorial on Powder X-ray Diffraction for Characterizing Nanoscale Materials. *ACS Nano* **2019**, *13*, 7359–7365. [CrossRef]
49. Zak, A.K.; Majid, W.H.A.; Abrishami, M.E.; Yousefi, R. X-ray analysis of ZnO nanoparticles by Williamson-Hall and size-strain plot methods. *Solid State Sci.* **2011**, *13*, 251–256. [CrossRef]
50. Withers, S.H.; Peale, R.E.; Schulte, A.F.; Braunstein, G.; Beck, K.M.; Hess, W.P.; Reeder, R.J. Broad distribution of crystal-field environments for Nd^{3+} in calcite. *Phys. Chem. Miner.* **2003**, *30*, 440–448. [CrossRef]
51. Qin, D.; Tang, W. Energy transfer and multicolor emission in single-phase $Na_5Ln(WO_4)_{4-z}(MoO_4)_z$:$Tb^{3+}$,$Eu^{3+}$ (Ln = La, Y, Gd) phosphors. *RSC Adv.* **2016**, *6*, 45376–45385. [CrossRef]
52. Pan, Y.; Wang, W.; Zhou, L.; Xu, H.; Xia, Q.; Liu, L.; Liu, X.; Li, L. F^--Eu^{3+} charge transfer energy and local crystal environment in Eu^{3+} doped calcium fluoride. *Ceram. Int.* **2017**, *43*, 13089–13093. [CrossRef]
53. Innocenzi, P. Infrared spectroscopy of sol-gel derived silica-based films: A spectra-microstructure overview. *J. Non Cryst. Solids* **2003**, *316*, 309–319. [CrossRef]
54. Osswald, J.; Fehr, K.T. FTIR spectroscopic study on liquid silica solutions and nanoscale particle size determination. *J. Mater. Sci.* **2006**, *41*, 1335–1339. [CrossRef]
55. Kreienborg, N.M.; Merten, C. How to treat C-F stretching vibrations? A vibrational CD study on chiral fluorinated molecules. *Phys. Chem. Chem. Phys.* **2019**, *21*, 3506–3511. [CrossRef]
56. Aguiar, H.; Serra, J.; González, P.; León, B. Structural study of sol-gel silicate glasses by IR and Raman spectroscopies. *J. Non Cryst. Solids* **2009**, *355*, 475–480. [CrossRef]
57. Song, C.; Dong, X. Preparation and Characterization of Tetracomponent $ZnO/SiO_2/SnO_2/TiO_2$ Composite Nanofibers by Electrospinning. *Adv. Chem. Eng.* **2012**, *2*, 108–112. [CrossRef]
58. Li, G.; Zhu, T.; Deng, Z.; Zhang, Y.; Jiao, F.; Zheng, H. Preparation of Cu-SiO_2 composite aerogel by ambient drying and the influence of synthesizing conditions on the structure of the aerogel. *Sci. Bull.* **2011**, *56*, 685–690. [CrossRef]
59. Gökçe, M.; Şentürk, U.; Uslu, D.K.; Burgaz, G.; Şahin, Y.; Gökçe, A.G. Investigation of europium concentration dependence on the luminescent properties of borogermanate glasses. *J. Lumin.* **2017**, *192*, 263–268. [CrossRef]
60. Binnemans, K. Interpretation of europium(III) spectra. *Coord. Chem. Rev.* **2015**, *295*, 1–45. [CrossRef]
61. Pisarski, W.A.; Pisarska, J.; Zur, L.; Goryczka, T. Structural and optical aspects for Eu^{3+} and Dy^{3+} ions in heavy metal glasses based on PbO-Ga_2O_3-XO_2 (X = Te, Ge, Si). *Opt. Mater.* **2013**, *35*, 1051–1056. [CrossRef]
62. Hurenkamp, J.H.; de Jong, J.J.D.; Browne, W.R.; van Esch, J.H.; Feringa, B.L. Tuning energy transfer in switchable donor-acceptor systems. *Org. Biomol. Chem.* **2008**, *6*, 1268–1277. [CrossRef]
63. Sołtys, M.; Pisarska, J.; Leśniak, M.; Sitarz, M.; Pisarski, W.A. Structural and spectroscopic properties of lead phosphate glasses doubly doped with Tb^{3+} and Eu^{3+} ions. *J. Mol. Struct.* **2018**, *1163*, 418–427. [CrossRef]
64. Tomina, V.V.; Stolyarchuk, N.V.; Katelnikovas, A.; Misevicius, M.; Kanuchova, M.; Kareiva, A.; Beganskienė, A.; Melnyk, I.V. Preparation and luminescence properties of europium(III)-loaded aminosilica spherical particles. *Coll. Surf. A* **2021**, *608*, 125552. [CrossRef]
65. Żur, L.; Pisarska, J.; Pisarski, W.A. Terbium -doped heavy metal glasses for green luminescence. *J. Rare Earth.* **2011**, *29*, 1198–1200. [CrossRef]
66. Bredol, M.; Gutzov, S. Effect of germanium-codoping on the luminescence of terbium doped silica xerogel. *Opt. Mater.* **2002**, *20*, 233–239. [CrossRef]
67. Szpikowska-Sroka, B.; Pawlik, N.; Goryczka, T.; Bańczyk, M.; Pisarski, W.A. Influence of activator concentration on green-emitting Tb^{3+}-doped materials derived by sol-gel method. *J. Lumin.* **2017**, *188*, 400–408. [CrossRef]
68. Parchur, A.K.; Prasad, A.I.; Ansari, A.A.; Rai, S.B.; Ningthoujam, R.S. Luminescence properties of Tb^{3+}-doped $CaMoO_4$ nanoparticles: Annealing effect, polar medium dispersible, polymer film and core-shell formation. *Dalton Trans.* **2012**, *41*, 11032–11045. [CrossRef] [PubMed]
69. Secu, C.E.; Bartha, C.; Polosan, S.; Secu, M. Thermally activated conversion of a silicate gel to an oxyfluoride glass ceramic: Optical study using Eu^{3+} probe ion. *J. Lumin.* **2014**, *146*, 539–543. [CrossRef]
70. Van Dijk, J.M.F.; Schuurmans, M.F.H. On the nonradiative and radiative decay rates and a modified exponential energy gap law for 4f-4f transitions in rare-earth ions. *J. Chem. Phys.* **1983**, *78*, 5317–5323. [CrossRef]
71. Xia, Z.; Zhuang, J.; Liao, L. Novel red-emitting $Ba_2Tb(BO_3)_2Cl$:Eu phosphor with efficient energy transfer for potential application in white light-emitting diodes. *Inorg. Chem.* **2012**, *51*, 7202–7209. [CrossRef]

72. Gopi, S.; Jose, S.K.; Sreeja, E.; Manasa, P.; Unnikrishnan, N.V.; Cyriac, J.; Biju, P.R. Tunable green to red emission via Tb sensitized energy transfer in Tb/Eu co-doped alkali fluoroborate glass. *J. Lumin.* **2017**, *192*, 1288–1294. [CrossRef]
73. Podhorodecki, A.; Banski, M.; Misiewicz, J.; Afzaal, M.; O'Brien, P.; Chad, D.; Wang, X. Multicolor light emitters based on energy exchange between Tb and Eu ions co-doped into ultrasmall β-$NaYF_4$ nanocrystals. *J. Mater. Chem.* **2012**, *22*, 5356–5361. [CrossRef]
74. Qin, X.; Shen, L.; Liang, L.; Han, S.; Yi, Z.; Liu, X. Suppression of Defect-Induced Quenching via Chemical Potential Tuning: A Theoretical Solution for Enhancing Lanthanide Luminescence. *J. Phys. Chem. C* **2019**, *123*, 11151–11161. [CrossRef]
75. Nicoara, I.; Munteanu, M.; Preda, E.; Stef, M. Some dielectric and optical properties of ErF_3-doped CaF_2 crystals. *J. Cryst. Growth* **2008**, *310*, 2020–2025. [CrossRef]
76. Trejo-García, P.M.; Palomino-Merino, R.; De la Cruz, J.; Espinosa, J.E.; Aceves, R.; Moreno-Barbosa, E.; Moreno, O.P. Luminescent Properties of Eu^{3+}-Doped Hybrid SiO_2-PMMA Material for Photonic Applications. *Micromachines* **2018**, *9*, 441. [CrossRef] [PubMed]
77. Chen, J.; Meng, Q.; May, P.S.; Berry, M.T.; Lin, C. Sensitization of Eu^{3+} luminescence in Eu:YPO_4 nanocrystals. *J. Phys. Chem. C* **2013**, *117*, 5953–5962. [CrossRef]
78. Werts, M.H.V.; Jukes, R.T.F.; Verhoeven, J.W. The emission spectrum and the radiative lifetime of Eu^{3+} in luminescent lanthanide complexes. *Phys. Chem. Chem. Phys.* **2002**, *4*, 1542–1548. [CrossRef]
79. Çetin, N.E.; Korkmaz, Ş.; Elmas, S.; Ekem, N.; Pat, S.; Balbağ, M.Z.; Tarhan, E.; Temel, S.; Özmumcu, M. The structural, optical and morphological properties of CaF_2 thin films by using Thermionic Vacuum Arc (TVA). *Mater. Lett.* **2013**, *91*, 175–178. [CrossRef]
80. Rehmer, A.; Scheurell, K.; Kemnitz, E. Formation of nanoscopic CaF_2 via a fluorolytic sol- gel process for antireflective coatings. *J. Mater. Chem. C* **2015**, *3*, 1716–1723. [CrossRef]
81. Sun, J.; Wang, H.; Zhang, Y.; Zheng, Y.; Xu, Z.; Liu, R. Structure and luminescent properties of electrodeposited Eu^{3+}-doped CaF_2 thin films. *Thin Solid Film* **2014**, *562*, 478–484. [CrossRef]